

Manuscript Supplement

This supplement provides additional context for the main paper and is divided into the following sections:

S1 - Geomorphic Context (including detailed assessment of paired ^{14}C - ^{10}Be nuclide diagrams and impact of in situ ^{14}C production by muons in the subsurface) **S2** Additional Sensitivity Analyses, **S3** - Comparison of excess scatter of in situ ^{14}C and ^{10}Be data from Mt Murphy, **S4** - Assessment of Mt Murphy quartz separates impact on in situ ^{14}C reproducibility and **S5** - Holocene filter age vs elevation plots and paired nuclide diagrams.

Supplement S1: Geomorphic Context

Here, we detail the geomorphic context for each sample at Mt Murphy for which a paired ^{14}C - ^{10}Be nuclide measurement has been performed. A full site description of scoria cone can be found in Adams et al., (2022). A site description of both Turtle Rock and Notebook Cliffs can be found in Johnson et al., (2020).

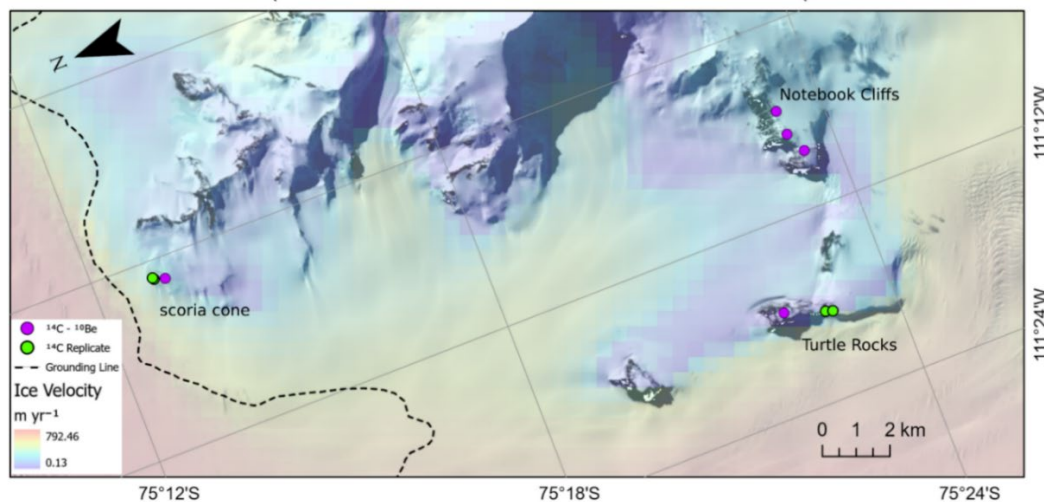


Figure S1. Mt Murphy sites and locations measured for both in situ ^{14}C and ^{10}Be displayed in the context of local ice velocities. Landsat-9 image from the online Data Pool, courtesy of the NASA EOSDIS Land Processes Distributed Active Archive Center (LP DAAC). Ice flow speeds are overlain to improve visualisation of ice localised ice flow and were downloaded from MEaSUREs InSAR-Based Antarctica Ice Velocity Dataset Version 2 (Mouginot et al., 2012, 2017; Rignot et al., 2011a, 2011b) [last accessed 25.05.2023]. Grounding line from (Milillo et al., 2022).

TURTLE ROCK

Many erratic boulders and cobbles have been recovered from Turtle Rock (Johnson et al., 2020). The lowest terrace from where TUR-117 and TUR-132 were recovered is relatively flat and also hosts the greatest density of erratics from anywhere visited so far in the Amundsen Sea Embayment (Johnson et al., 2020).

TUR-117 (451 m a. s. l.): Granite erratic boulder recovered from relatively flat surface of the lower Turtle Rock platform. The lithology is exotic, and the shape is well-rounded suggesting long-distance subglacial transport, the degree of weathering is minor.

TUR-123 (639 m a. s. l.): Granite erratic boulder recovered from the upper slope of Turtle Rock. The lithology is exotic, and the shape is sub-rounded suggesting long-distance subglacial transport, degree of weathering is moderate.

TUR-132 (446 m a. s. l.): Granite erratic boulder recovered from relatively flat surface of the lower Turtle Rock platform. Lithology is exotic and the shape is sub-rounded suggesting long-distance subglacial transport, the degree of weathering is moderate to slight.

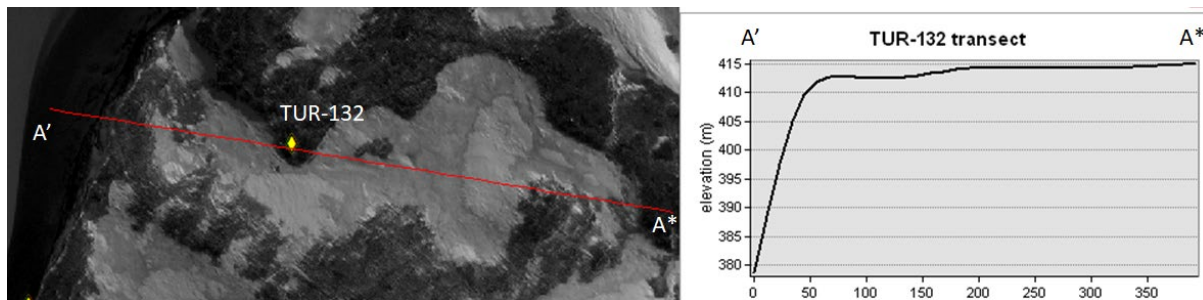


Figure S2. TUR 132 sample location at Turtle Rock and transect line with E-W topographic profile. Satellite imagery from DigitalGlobe products, © WorldView-2 DigitalGlobe, Inc., a Maxar company.

SCORIA CONE

CIN samples were recovered from a parasitic scoria cone ~ 1.5 km west of Kay Peak ridge which comprises of two separate outcrops: A (Fig S3) and B (Fig S4). There is evidence to suggest the lower outcrop was covered by ice for a non-zero duration during the late Holocene. The scoria cone outcrops are well described in (Adams et al., 2022).

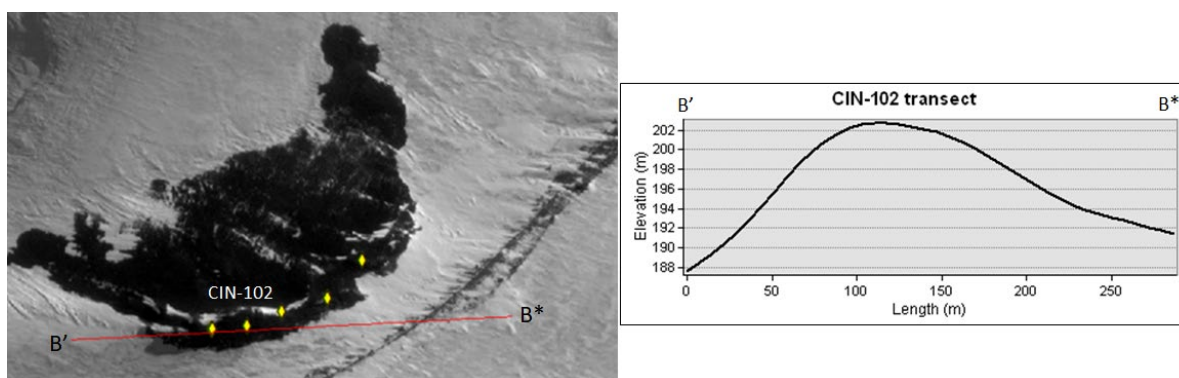


Figure S3. CIN-102 sample location at scoria cone outcrop A and transect with E-W topographic profile. Satellite imagery from DigitalGlobe products, © WorldView-2 DigitalGlobe, Inc., a Maxar company.

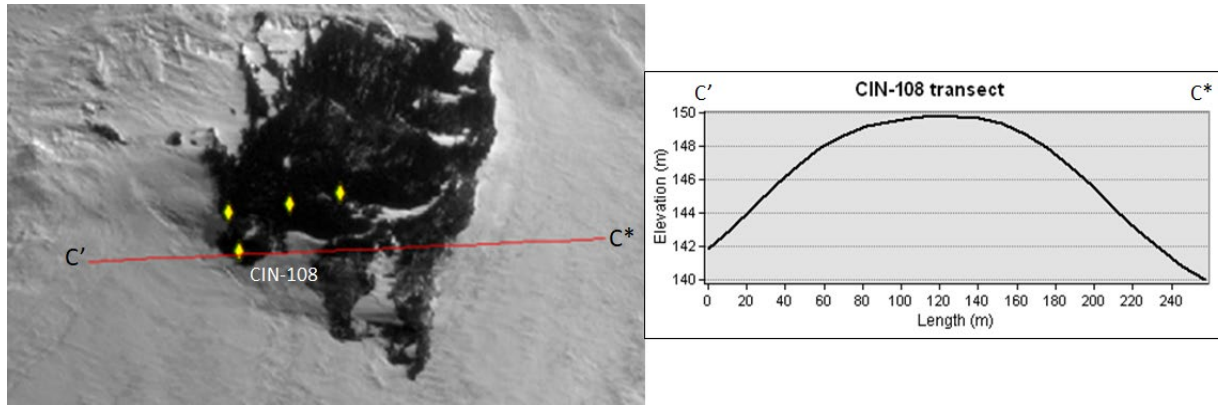


Figure S4. CIN-108 sample location at scoria cone outcrop B and transect line with E-W topographic profile. Satellite imagery from DigitalGlobe products, © WorldView-2 DigitalGlobe, Inc., a Maxar company.

CIN-102 (239 m a. s. l.) Gneiss erratic of similar lithology to Kay Peak, so there is potential it has been transported from a short distance. The shape of the erratic is subrounded to subangular, and the degree of weathering on the sample is moderate.

CIN-108 (181 m a.s.l): Sub-rounded erratic of exotic granite lithology, suggesting probable long-distance transport, displays a moderate degree of weathering.

CIN-112 (179 m a. s. l.): Sub-rounded erratic of aplite lithology, suggesting probable long-distance transport, although a small amount of aplite has also been documented at Kay Peak, sample displays a moderate degree of weathering.

NOTEBOOK CLIFFS

The NOT samples were recovered from a broad basaltic platform at ~ 900 m a. s. l at the top of Notebook Cliffs (Johnson et al., 2020), the outcrop also contains evidence of hyaloclastite. Cliffs on the northern side are near vertical, but the top is relatively flat and of high elevation. Notably many fewer erratics at Notebook Cliffs than exhibited at lower elevation sites such as nearby Icefall Nunatak (Johnson et al., 2020).

NOT-103 (852 m a. s. l.): Subangular erratic of granite lithology, lithology is exotic at Notebook Cliffs which is comprised of mafic rock (basalt and hyaloclastite). Degree of weathering is minor.

NOT-104 (893 m a. s. l.): Subangular erratic of granite lithology, Notebook Cliffs is comprised of mafic rock (basalt and hyaloclastite), so lithology is exotic. Sample is moderately weathered with evidence of slight pitting on its surface.

NOT-107 (885 m a. s. l.): Subangular erratic of granite lithology, Notebook Cliffs is comprised of mafic rock (basalt and hyaloclastite), so lithology is exotic. Degree of weathering is minor.

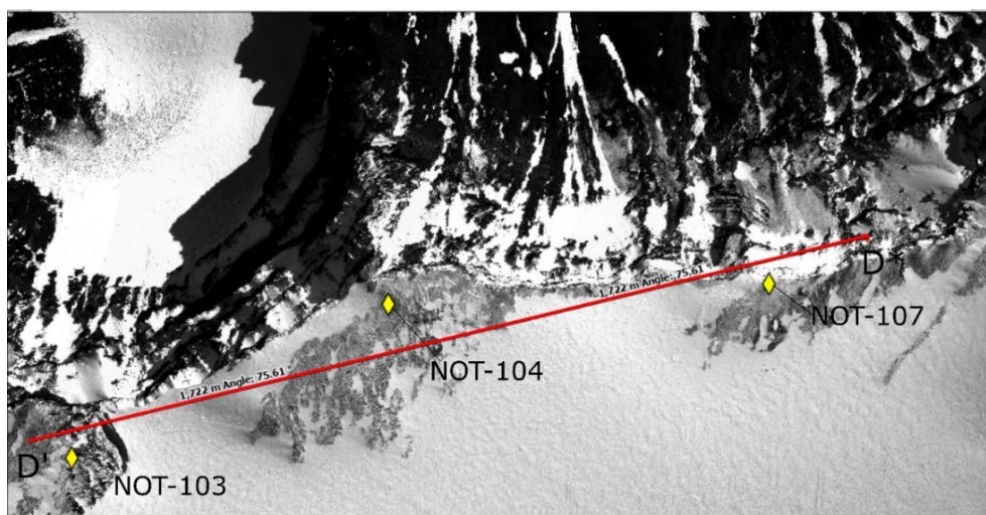


Figure S5. Locations of samples NOT-103, NOT-104 and NOT-107 at Notebook Cliffs. Satellite imagery from DigitalGlobe products, © WorldView-2 DigitalGlobe, Inc., a Maxar company.

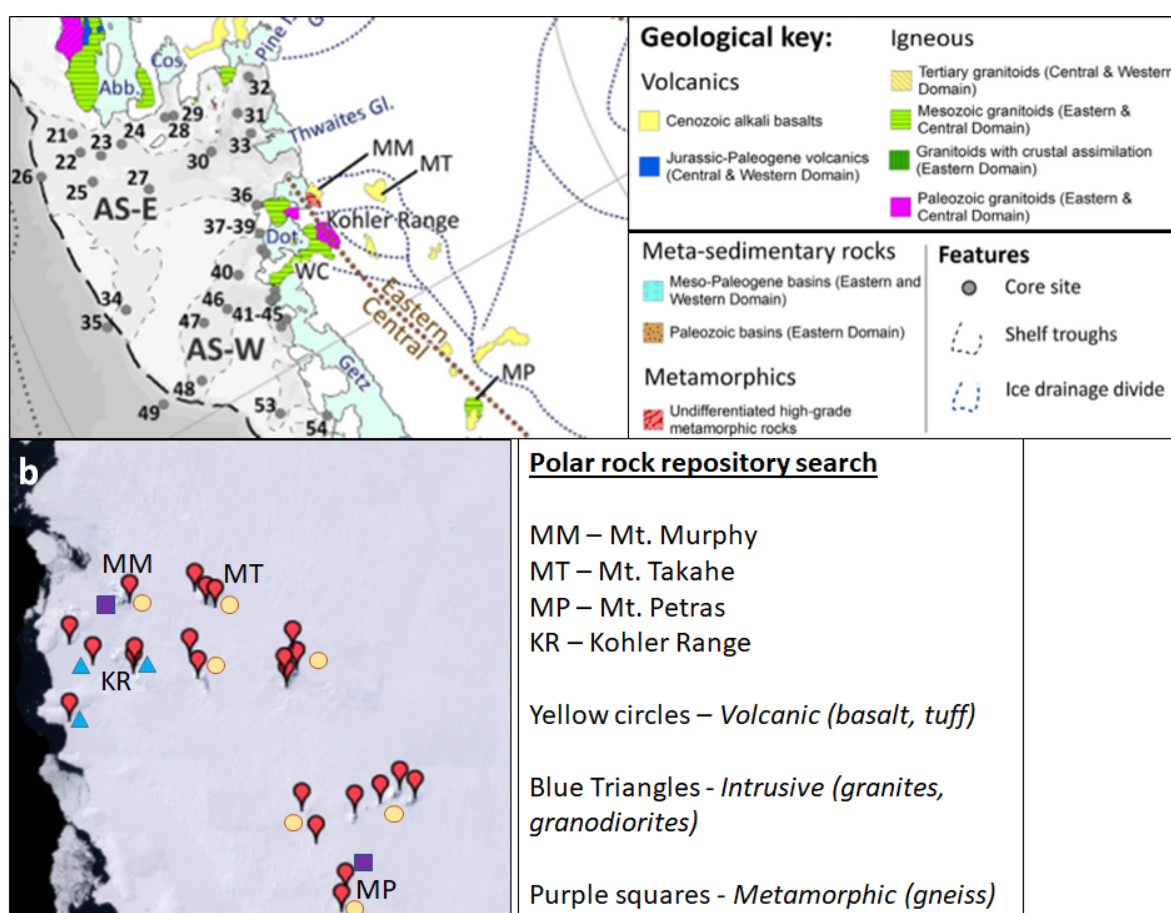


Figure S6. Panel (a) shows map from provenance study compiling lithology of major outcrops of exposed rock, blue dotted lines represent present ice divides, dashes black line represents shelf edge, taken from (Simões Pereira et al., 2018). Panel (b) polar rock repository database search of areas of exposed rock upstream of Mt Murphy as well as in the wider area of the Amundsen Sea Embayment and Marie Byrd Land. Rock sample data points courtesy of the Polar Rock Repository Database <https://prr.osu.edu/> [Accessed 22.04.24]

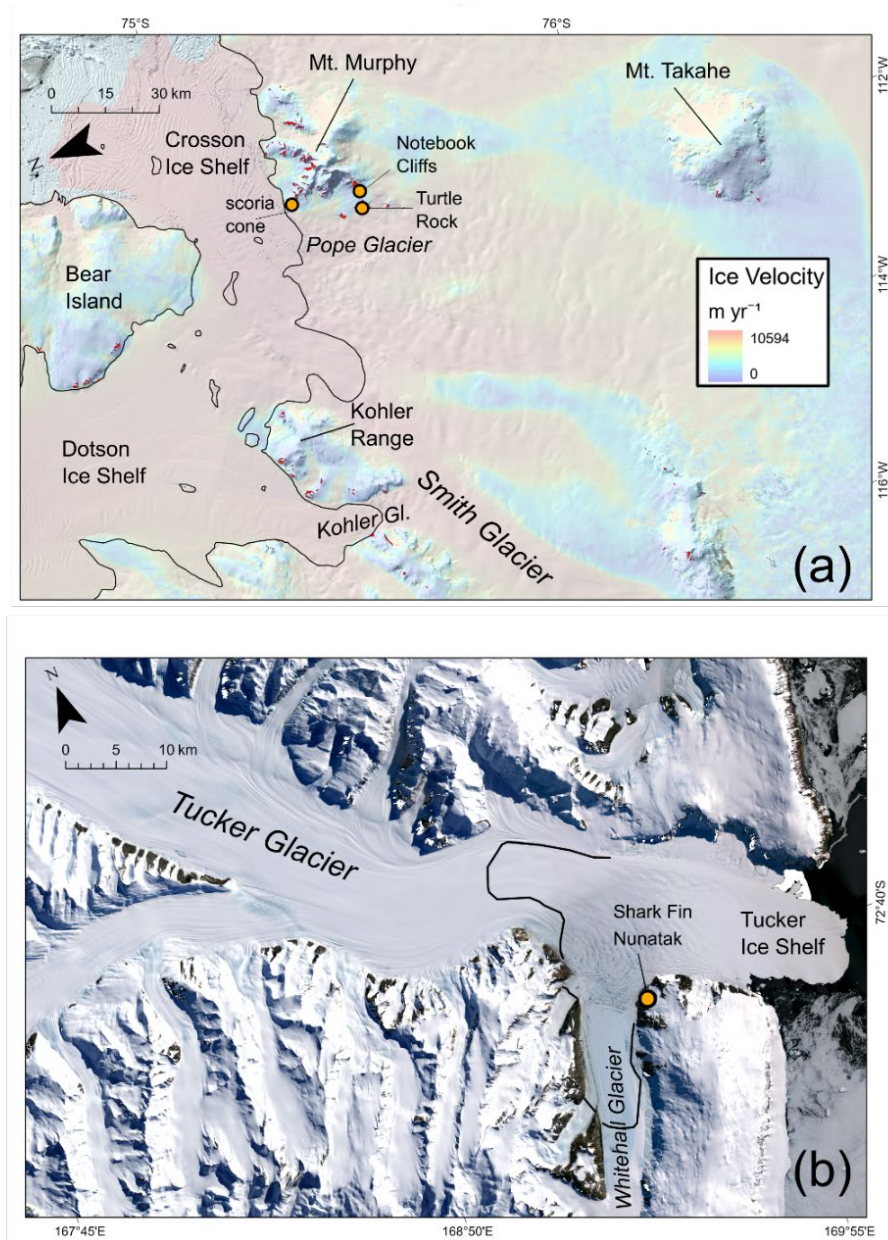


Figure S7. Regional comparison of Mt Murphy panel (a) and Tucker Glacier panel (b) demonstrating the comparative topographic isolation of Mt Murphy compared to Tucker Glacier. Orange circles show paired in situ ¹⁴C-¹⁰Be sample sites mentioned in the text. Black lines in both images show locations of grounding lines determined by differential satellite radar interferometry (Rignot et al., 2011a). Ice flow speed is displayed to improve visualisation of ice streams for panel (a) and was downloaded from from MEaSUREs InSAR-Based Antarctica Ice Velocity dataset Version 2 (Mouginot et al., 2012, 2017; Rignot et al., 2011b) [last accessed 25.05.2023]. To improve visualisation exposed rock outcrops in Panel (a) are displayed red using the Antarctic rock outcrop dataset (Burton-Johnson et al., 2016). Both satellite images are sourced from Landsat Image Mosaic of Antarctica (LIMA; lima.usgs.gov).

95 **Figure S8.** Photos of samples analysed for both ^{10}Be and in situ ^{14}C in this study. Exposure ages with 1σ external uncertainties for ^{10}Be , in situ ^{14}C and in situ ^{14}C replicate measurements are shown below each image.



NOT-103

^{10}Be - 9.4 ± 0.6 ka

^{14}C - 3.8 ± 0.4 ka



NOT-104

^{10}Be - 8.6 ± 0.6

^{14}C - 4.1 ± 0.4 ka



NOT-107

^{10}Be - 8.9 ± 0.9

^{14}C - 5.2 ± 0.6 ka



TUR-117

^{10}Be - 6.7 ± 0.5 ka

^{14}C - 3.1 ± 0.3 ka

$^{14}\text{C R}$ - 8.2 ± 1.1 ka



TUR-123

^{10}Be - 10.3 ± 0.7 ka

^{14}C - 3.8 ± 0.4 ka



TUR-132

^{10}Be - 6.6 ± 0.5 ka

^{14}C - 7.9 ± 1.0 ka

$^{14}\text{C R}$ - 7.4 ± 0.9 ka



CIN-102

^{10}Be - 7.5 ± 0.5 ka

^{14}C - 9.0 ± 1.3 ka



CIN-108

^{10}Be - 6.2 ± 0.4 ka

^{14}C - 6.3 ± 0.7 ka

$^{14}\text{C R}$ - 7.8 ± 1.0 ka



CIN-112

^{10}Be - 6.6 ± 0.4 ka

^{14}C - 3.4 ± 0.3 ka

$^{14}\text{C R}$ - 7.2 ± 0.9 ka

Supplement S1.2: Identifying sites with paired ^{14}C - ^{10}Be nuclide systematics resembling Mt Murphy

Focusing on the conditions surrounding each of the three endmember ^{14}C - ^{10}Be datasets may help explain our observations from the Mt Murphy paired ^{14}C - ^{10}Be dataset. Here, we provide a detailed examination of endmember sites where samples are dominated by Type 1, Type 2 and Type 3 ^{14}C - ^{10}Be concentration ratios (Fig. 6, main text), to determine if a link can be established between the geologic setting of such sites and the nature of their paired nuclide systematics. The Type 1 endmember ^{14}C - ^{10}Be dataset from KNS, Greenland, exhibits concordant ^{14}C - ^{10}Be exposure ages and ^{14}C - ^{10}Be ratios consistent with a simple exposure history (Young et al., 2021). Observations from the KNS study site are well documented, both historically back to the 1850's (Young et al., 2021 cf. Fig. 10) and presently (Young et al., 2021 cf. Fig. 2). As a result, observational uncertainties are minimal, which permits the maximum permissible duration of Holocene exposure to be constrained, in this case to ^{10}Be of 10.2 ± 0.2 ka (Young et al., 2021). The study in which this dataset was generated benefitted from local production rate calibration datasets from West Greenland for ^{10}Be and in situ ^{14}C (Young et al., 2014), ensuring that production rates and the ^{14}C - ^{10}Be production ratio were regionally constrained (Young et al., 2021). Finally, sources of analytical uncertainty of in situ ^{14}C were propagated for each sample based on long-term CRONUS-A measurements from LDEO where extraction took place (Lamp et al., 2019). All six samples without ^{10}Be inheritance possess in situ ^{14}C - ^{10}Be ratios that are indistinguishable and therefore imply a simple exposure history. In terms of accuracy, the ^{10}Be ages obtained from KNS are confirmed by concordant in situ ^{14}C ages. The Type 1 dataset from KNS is associated with well constrained concordant paired in situ ^{14}C - ^{10}Be exposure ages that permit the Holocene deglaciation history of the site to be reconstructed with high confidence. From the filter analysis of ICE-D, eight other sites display ^{14}C - ^{10}Be concentration ratios that are exclusively Type 1: Mario Zuchelli Station and Cape Marsh-Robertson Island from Antarctica (Goehring et al., 2019; Jeong et al., 2018) and six sites from elsewhere around the globe (see Table 4, main text). However, five of these eight sites all contain only one in situ ^{14}C - ^{10}Be pair each, which were extracted based on the Holocene search filter.

The Type 2 endmember dataset is taken from the Rhône Glacier exposure age dataset from the Swiss Alps (Goehring et al., 2011). Notebook Cliffs appears to be the only other dataset that exclusively exhibits Type 2 ^{14}C - ^{10}Be concentration ratios (Table 4, main text). Much like paired in situ ^{14}C - ^{10}Be ratios from Notebook Cliffs and paired in situ ^{14}C - ^{10}Be ratios based on the initial in situ ^{14}C measurements of TUR-117 and CIN-112 (Fig. 4a), the in situ ^{14}C - ^{10}Be ratios from Rhône Glacier plot within the area of complex exposure. The Rhône Glacier study effectively utilised the complex exposure and burial history of the samples uncovered from the forefield of the glacier to determine when it likely expanded and contracted during the Holocene (Goehring et al., 2011). Historical records aid with the interpretation of the Rhône Glacier exposure ages (much like at KNS) as the samples are known to have been covered in the recent past when the glacier expanded during the Little Ice Age (Goehring et al., 2011). The Rhône Glacier dataset is more straightforward to interpret than the Mt Murphy dataset because all ^{14}C - ^{10}Be exposure age pairs (except one outlier) plot below the steady erosion line. At Mt Murphy, apparent discordant and concordant ^{14}C - ^{10}Be paired exposure ages from the same elevation suggest that some, but not all, samples were shielded during the Holocene, requiring a complex geologic model.

The Type 3 endmember dataset from Sjögren Glacier - Site C (Balco and Schaefer, 2013) displays impermissible ^{14}C - ^{10}Be concentration ratios (when assuming a constant surface production rate). At Mt Murphy, no samples have impermissible ^{14}C - ^{10}Be ratios, but CIN-102, TUR-132 and particularly CIN-108-R display very high ^{14}C - ^{10}Be ratios (Fig. 4, main text). Exposure ages from Sjögren Glacier samples are bimodal. One group of mid-Holocene exposure ages (including replicates) decreases in age with elevation, from 4.8 ka at 120 m a. s. l. to 3.4 ka at 40 m a. s. l., whilst some samples suggest extremely recent exposure between just 200–500 years ago (Balco and Schaefer, 2013). From analysis of ^{10}Be ages, it was suggested that the site was fully deglaciated at 3.5–4.5 ka, partially covered again by thickening of the adjacent Boydell Glacier at or after ca 1.4 ka, and then deglaciated again between 1969 and the present (Balco and Schaefer, 2013). A complex exposure scenario at Sjögren Glacier may have, therefore, created specific conditions in which seemingly implausible in situ ^{14}C - ^{10}Be ratios can be explained geologically if samples at Sjögren Glacier Site C were buried under a thin layer of cold-based ice during the Holocene prior to more recent exposure. An impermissible in situ ^{14}C - ^{10}Be concentration ratio (when assuming surface production) could therefore become plausible if samples at Sjögren Glacier were subject to long periods of subsurface production during the Holocene or recent rapid exhumation from moderate depth (Rand and Goehring, 2019).

Supplement S1.3: Increased ^{14}C - ^{10}Be ratio by higher in situ ^{14}C subsurface production by muons relative to ^{10}Be

To better understand the high in situ ^{14}C - ^{10}Be ratios exhibited by CIN-108-R at Mt Murphy, as well as paired in situ ^{14}C - ^{10}Be isotope systematics more generally, we further investigate the impermissible in situ ^{14}C - ^{10}Be ratios at Sjögren Glacier. We also choose to investigate this dataset further because 1) the close geomorphic resemblance of the Sjögren Glacier Site C to the scoria cone site at Mt Murphy and 2) the high number of replicate in situ ^{14}C measurements from Sjögren Glacier. We, therefore, model scenarios where samples are subject to either rapid exhumation from ice, or prolonged burial under ice, leading to higher in situ ^{14}C production relative to ^{10}Be production in the subsurface (see section 1.1, main text). In both scenarios the in situ ^{14}C nuclide concentration is expected to increase relative to ^{10}Be and may explain impermissible Type 3 ^{14}C - ^{10}Be concentration ratios observed at Sjögren Glacier.

We first model rapid exhumation of a sample from beneath overlying ice, which is equivalent to increasing the erosion rate, to investigate if this scenario would yield in situ ^{14}C - ^{10}Be ratios comparable to ratios observed in Sjögren Glacier samples (Fig. 7a, main text). We observe that an increase in the glacial exhumation rate to between 1000–2000 mm kyr⁻¹ results in higher modelled ^{14}C - ^{10}Be ratios (≥ 1.2), comparable to ratios observed in the Sjögren Glacier samples. Faster glacial exhumation rates, however, also result in modelled ^{10}Be concentrations of < 2000 at g⁻¹, considerably lower than ^{10}Be concentrations measured in the Sjögren Glacier samples. At slower glacial exhumation rates of 300–400 mm kyr⁻¹, the modelled ^{10}Be concentration is comparable to concentrations at Sjögren Glacier, but the modelled ^{14}C - ^{10}Be ratio is < 1 , which is much lower than the high ^{14}C - ^{10}Be ratio of most Sjögren Glacier samples. Increasing ice surface thinning (erosion rates) above 300–400 mm kyr⁻¹ leads to resulting modelled in situ ^{14}C - ^{10}Be nuclide concentration ratios plotting above the constant exposure line, but only when ^{10}Be concentrations are low (see Fig. 7a, main text). None of the Sjögren Glacier samples, however, exhibit low ^{10}Be nuclide concentrations (range; 18070 ± 591 to 27670 ± 686 at g⁻¹). The surface nuclide concentration is inversely proportional to the rate of exhumation of the sample from overlying ice, meaning there is an intersection between maximising the duration of greater ^{14}C production over an integrated depth and minimising the impact of the faster rate of decay of ^{14}C relative to ^{10}Be . Consequently, high ^{14}C - ^{10}Be ratios are only permitted when ^{10}Be concentration in a sample is low, due to the increasingly fast removal of accumulated nuclides at higher rates of glacial exhumation of rock samples.

We model for a second scenario whereby a sample is buried at specific depths of 1, 2 and 5 metres under ice over Holocene timescales (Fig. 7b, main text). For this scenario, we observe that significant burial at depths below 2–3 metres are required to generate a high modelled ^{14}C - ^{10}Be ratio, which is comparable with ratios observed in Sjögren Glacier samples. Burial under 5 metres of ice increases the ^{14}C - ^{10}Be ratios to match the highest ratios observed at Sjögren Glacier. However, the ^{10}Be nuclide concentration is extremely low at these ratios (< 1000 at g⁻¹).

Modelling prolonged burial of a sample at depths greater than ~ 2.5 –3 metres under ice leads to high ^{14}C - ^{10}Be ratios comparable to ^{14}C - ^{10}Be ratios of Sjögren Glacier samples (Fig. 7b, main text). The high ^{14}C - ^{10}Be production ratio at depth is due to the almost complete attenuation of the high energy neutron flux (Dunai, 2010) and dominance of nuclide production due to negative muon capture (Balco, 2017; Heisinger et al., 2002). However, high ^{14}C - ^{10}Be ratios are again only observed when the ^{10}Be concentration is low (< 1000 at g⁻¹). Over longer burial durations where greater concentrations of ^{10}Be accumulate the high in situ ^{14}C to ^{10}Be production ratio is offset by the much faster decay rate of in situ ^{14}C relative to ^{10}Be . In addition, the likely exposure history at Sjögren Glacier Site C indicated from ^{10}Be ages is 2–3 kyr of initial surface exposure followed by shallow burial under a thin ice layer at 1.4 ka (Balco and Schaefer, 2013). In this case, the significant duration of surface exposure precludes the high in situ ^{14}C - ^{10}Be concentration ratios observed in the Sjögren Glacier samples because of the significant quantities of in situ ^{14}C and ^{10}Be atoms already accumulated in the sample at the surface production ratio.

In summary, observed ratios of in situ ^{14}C - ^{10}Be relative to ^{10}Be concentrations at Sjögren Glacier cannot be reconciled by either faster rates of glacial exhumation of samples buried below the ice or prolonged burial at shallow to moderate ice thicknesses (1–5 metres). In both scenarios, if the concentration of ^{10}Be atoms is low, high modelled ^{14}C - ^{10}Be ratios comparable to the in situ ^{14}C - ^{10}Be concentration ratios in Sjögren Glacier samples are observed. However, as soon as ^{10}Be nuclide concentrations exceed 1000–2000 at g⁻¹, high ^{14}C - ^{10}Be ratios are no longer observed due to 1) high erosion rates rapidly removing accumulated nuclides and or 2) the more rapid decay of in situ ^{14}C relative to ^{10}Be offsetting the higher ^{14}C - ^{10}Be subsurface production ratio.

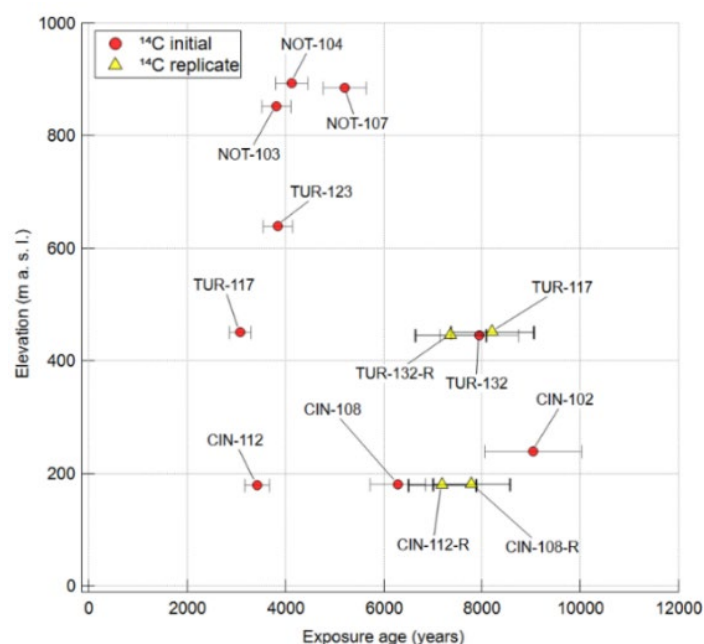


Figure S9. Plot of in situ ^{14}C ages vs elevation comparing in situ ^{14}C exposure ages calculated from both initial and replicate in situ ^{14}C concentrations. Ages derived from initial in situ ^{14}C concentrations are depicted by red circles and ages derived from replicate concentrations by yellow triangles. In situ ^{14}C exposure ages are plotted with 1σ internal uncertainties calculated from the 6 % measurement uncertainty applied to in situ ^{14}C concentrations (see Table 1, main text). Replicate in situ ^{14}C uncertainty bars displayed with thicker lines.

Mt Murphy alternative blank

We present a further sensitivity analysis on the impact of altering the blank correction value on replicate in situ ^{14}C concentrations (and exposure ages). We use an alternative blank correction of $3.99 \pm 1.25 \times 10^4$ atoms ($n = 5$) based on the mean and standard deviation of process blanks reported from Tulane laboratory from 03/08/2021 – 12/10/2021 (see Figure S10b). These process blanks represent a change from “thick” 3 mm tubes to a “thin” 1.5 mm mullite tube for ^{14}C extraction (Table S5, Balco et al., 2023) and are the blank data closest in time to replicate in situ ^{14}C concentrations. The alternative blank (BI-2) resulted in poorer reproducibility of initial and replicate in situ ^{14}C ages (3 of 4 did not reproduce at 1σ external uncertainty) and discordance between 3 of 4 replicate in situ ^{14}C ages and corresponding ^{10}Be ages (Figure S10b). Therefore, this additional sensitivity analysis does not alter our conclusions from results using the blank correction values of $4.53 \pm 3.50 \times 10^4$ atoms and $7.14 \pm 3.50 \times 10^4$ atoms reported by Tulane.

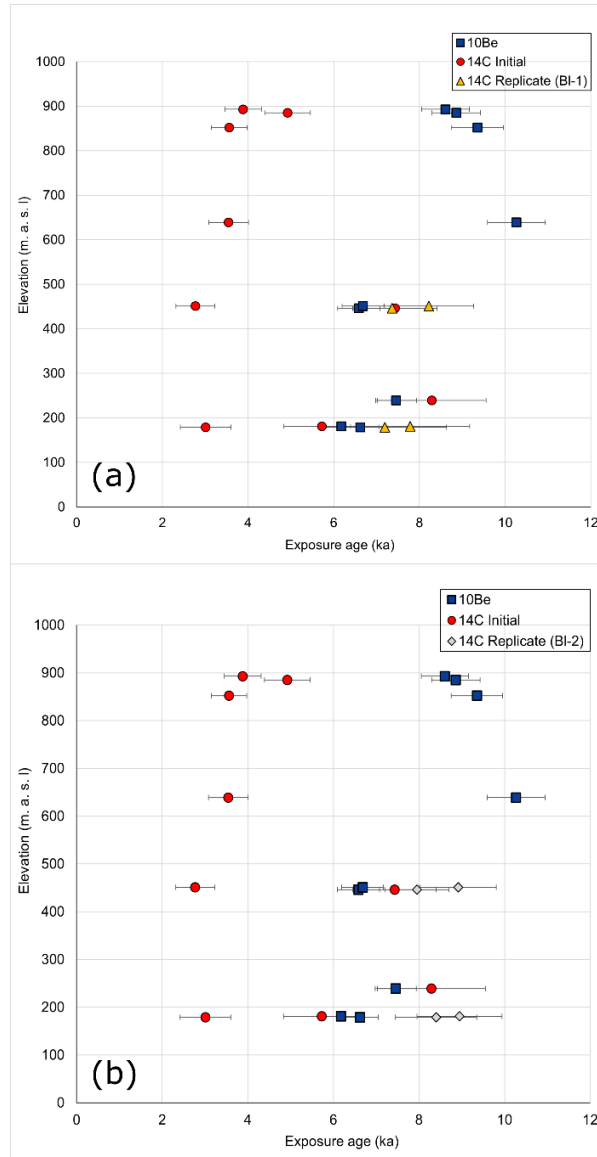
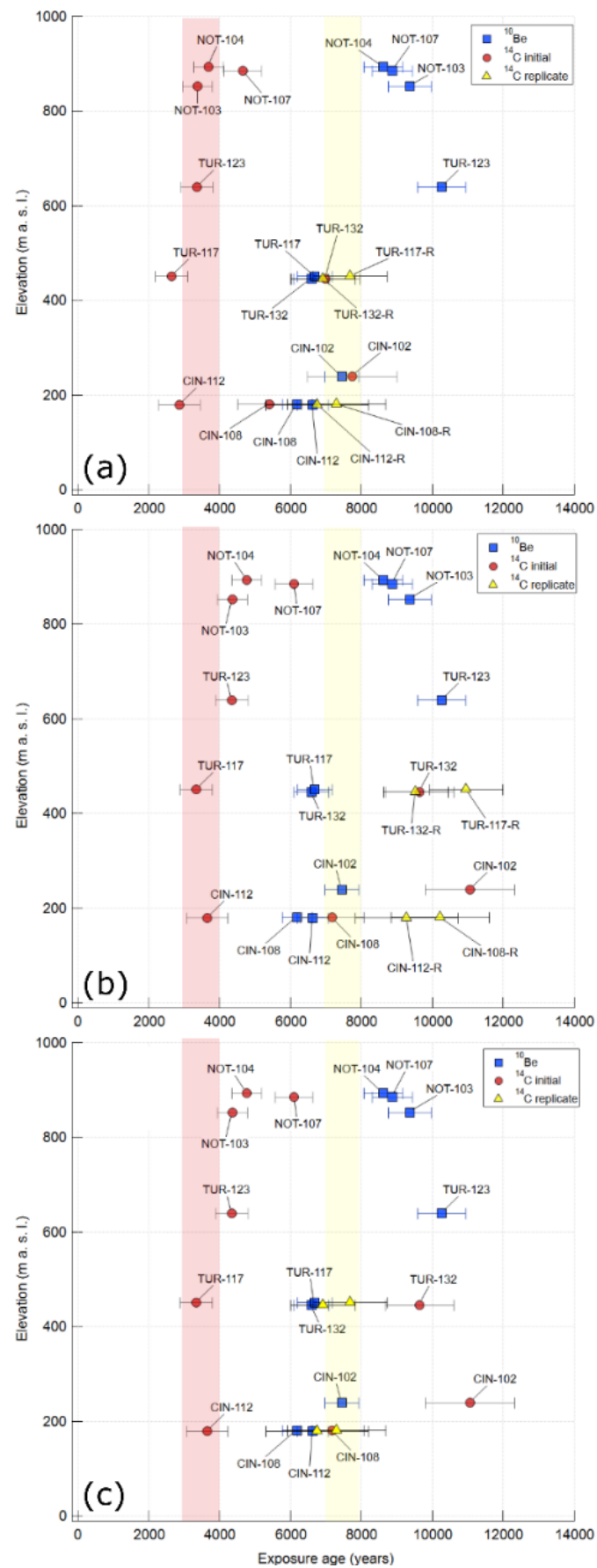


Figure S10. Additional sensitivity analysis comparing (a) replicate in situ ^{14}C concentrations corrected using blank value of $7.14 \pm 3.50 \times 10^4$ atoms presented in Section 4.2, which represent the blank value reported by Tulane, and the standard deviation of all process blanks measured at Tulane from 2019-2021 (BI-1) and (b) blank correction of $3.99 \pm 1.25 \times 10^4$ atoms based on mean and standard deviation of process blanks reported from Tulane laboratory from 03/08/2021 – 12/10/2021. These are the closest process blanks reported in time to in situ ^{14}C replicate measurements and represent a change from a “thick” 3 mm mullite tube to a “thin” 1.5 mm mullite tube for ^{14}C extraction (BI-2). Note initial in situ ^{14}C concentrations are corrected using a blank of $7.44 \pm 4.16 \times 10^4$ atoms ($n = 6$, mean and standard deviation of process blanks bracketing initial measurements) in both plots.

Figure S11 (Overleaf): CRONUS-A normalization sensitivity test. Recalculated in situ ^{14}C concentrations normalized to (a) CRONUS-A = $5.88 \pm 0.59 \times 10^5$ at g^{-1} , the mean and standard deviation of all CRONUS-A measurements ($n = 18$) reported from Tulane CNL and (b) CRONUS-A = $7.11 \pm 0.10 \times 10^5$ at g^{-1} , the last reported CRONUS-A extraction from Tulane CNL (12/03/2021) which coincides with the extraction period of initial ^{14}C measurements (02/03/2021 – 10/04/2021). (c) normalizes initial in situ ^{14}C concentrations by the CRONUS-A value of $7.11 \pm 0.10 \times 10^5$ at g^{-1} and replicate ^{14}C concentrations by the CRONUS-A value of $5.88 \pm 0.59 \times 10^5$ at g^{-1} . Fixed 1 kyr windows are shown on each figure to more clearly demonstrate the shift in i) young in situ ^{14}C exposure ages (shaded red) and ii) in situ ^{14}C ages calculated from replicate measurements (shaded yellow).

Mt Murphy CRONUS-A



Sjögren Glacier Sensitivity Analysis

Here, we perform a sensitivity analyses on initial and replicate in situ ^{14}C concentrations measured from Sjögren Glacier. A CRONUS-A concentration of 5.18×10^5 atoms g^{-1} was measured close to initial in situ ^{14}C extractions from Sjögren Glacier (25/09/2018 – 19/10/2018) and a CRONUS-A concentration of 6.69×10^5 atoms g^{-1} close to the period of replicate in situ ^{14}C measurements (04/09/2020 – 30/09/2020). We renormalize the Sjögren Glacier in situ ^{14}C concentrations (based on the value of $6.12 \pm 0.32 \times 10^5$ atoms g^{-1} reported in Goehring et al., (2019) by the CRONUS-A values closest in time to initial and replicate samples respectively. We also assign the same blanket 10 % uncertainty based on the standard deviation of all CRONUS-A data reported from Tulane as we did for the Mt Murphy in situ ^{14}C concentrations. Replicate measurements for 10-LAR-018-SJO and 10-LAR-024-SJO still do not reproduce within uncertainty. The same 2 of 3 in situ ^{14}C concentrations measured in samples 10-LAR-018-SJO and 10-LAR-024- from Sjögren Glacier which did not overlap within the $\pm 6\%$ uncertainty (Fig. 8, main text) still do not reproduce. Therefore, our conclusions drawn from these in situ ^{14}C replicate measurements from Sjögren Glacier are unchanged.

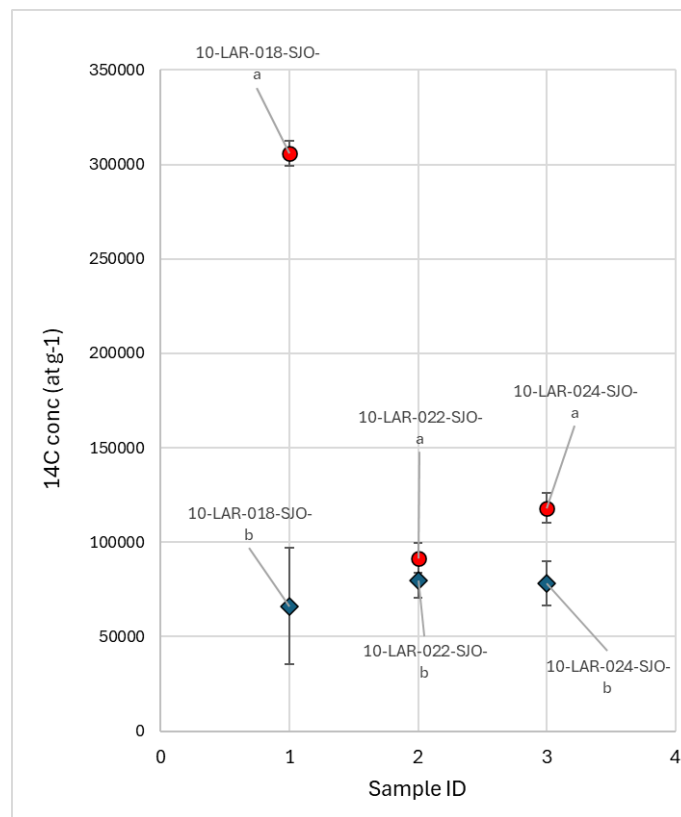
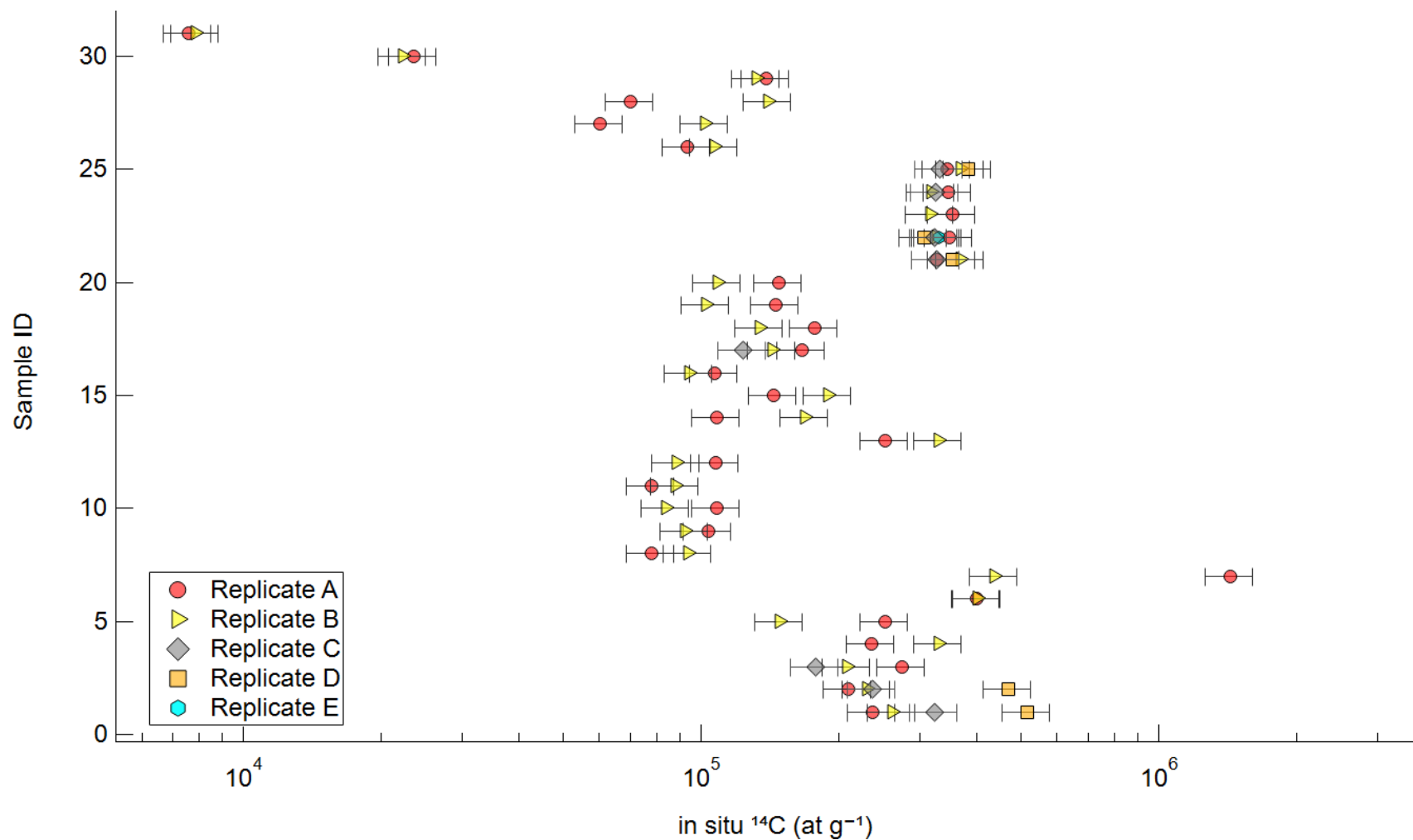


Figure S12: Sjögren Glacier in situ ^{14}C concentrations renormalized to CRONUS-A measurements made closest in time to in situ ^{14}C extractions of Sjögren Glacier samples. We apply a 10 % uncertainty to the in situ ^{14}C concentrations.



265

Figure S13. In situ ^{14}C concentrations in ICE-D for which one or more replicate measurements have been made on the same sample ($n = 31$). Same samples are displayed as in Fig. 8 (main text) showing 2σ uncertainty on measurement concentrations based on reproducibility analysis of CRONUS-A at Tulane extraction laboratory. Graph indicates that 15 of 31 samples continue to exhibit one or more in situ ^{14}C measurement concentrations which do not reproduce at 2σ .

Supplement S3: Comparison of excess scatter of in situ ¹⁴C and ¹⁰Be data from Mt Murphy

Due to the large scatter in ages observed from in situ ¹⁴C measurements along the elevation profile from Mt Murphy (Balco et al., 2023; Johnson et al., 2020), we chose to compare in situ ¹⁴C and ¹⁰Be scatter from the scoria cone and Kay Peak (see Fig. 1a). Using sites that are geographically proximal and at similar elevation minimises additional variation in non-paired exposure age measurements that can arise from inherent uncertainties in production rate scaling when comparing two nuclides. We calculated the error in excess of analytical uncertainty separately for both the ¹⁰Be dataset from scoria cone and in situ ¹⁴C dataset from Kay Peak using the following steps. First we performed a linear regression analyses of the age vs elevation distribution of the exposure ages to obtain the residuals of the least squared fit to the dataset (Bevington and Robinson, 1993). We then performed a bootstrap uncertainty analysis by resampling (sampling with replacement) the residuals determined from the original linear regression model. We fit a new regression model to the resampled data, resampling the original dataset 1000 times. We then calculated the excess scatter in our dataset using the standard deviation of the distribution of regression models determined from resampled residuals.

We omitted three ¹⁰Be exposure ages from erratic cobbles from Kay Peak that are all > ~10 ka from the statistical analysis because the original study identified inheritance in those samples (Johnson et al., 2020). We did not omit any of the in situ ¹⁴C ages from statistical analysis because all in situ ¹⁴C exposure ages postdate the onset of the Holocene (< 11.7 ka), indicating a negligible amount of nuclide inheritance. Data includes in situ ¹⁴C measured in bedrock samples from Kay Peak ridge ($n = 17$) and initial in situ ¹⁴C concentrations measured in erratics ($n = 3$) from scoria cone.

We then calculated the additional error in excess of AMS measurement uncertainty for both the in situ ¹⁴C sample set and the ¹⁰Be sample set using the following equation:

$$\text{Excess Uncertainty} = (S^2) - (\bar{x}\sigma^2) \quad \text{Eq. S3.1}$$

where S denotes the standard deviation of the in situ ¹⁴C or ¹⁰Be residuals, i.e., total scatter in each respective dataset (in years) and $\bar{x}\sigma$ refers to the average analytical uncertainty of the collective in situ ¹⁴C or ¹⁰Be exposure ages in each respective sample set (also in years).

In situ ¹⁴C and ¹⁰Be bootstrapping results from Mt Murphy

We now compare results from our statistical analysis of scoria cone and Kay Peak exposure age datasets. The in situ ¹⁴C derived line of best fit indicates deglaciation began at 7.1 ka (uncovering of surfaces at 350 m a. s. l.) and surfaces at 125 m a. s. l. were uncovered by 6.1 ka. The ¹⁰Be-derived line of best fit indicates that deglaciation (uncovering surfaces at 350 m a. s. l.) began slightly earlier, at 8.3 ka, with surfaces at 125 m a. s. l. uncovered slightly later, at 5.7 ka. The age range for deglaciation is similar for the two datasets, and the data broadly follow the same linear trend (Fig. S14). This similarity strongly suggests that an accurate chronology is being achieved with both nuclides at this site, and there is minimal inheritance in the samples. At 95 % confidence, the degree of scatter of the in situ ¹⁴C dataset (Fig. S14a) is greater than the ¹⁰Be dataset (Fig. S14b).

The in situ ¹⁴C sample set ($n = 20$) has a residual standard deviation of 1957 years and the ¹⁰Be sample set has a residual standard deviation of 225 years ($n = 12$) (Table S6). The average internal uncertainty of the in situ ¹⁴C exposure ages is 641 years, whilst the average internal uncertainty of the ¹⁰Be exposure ages is 222 years. The unquantified uncertainty remaining from scatter in the in situ ¹⁴C exposure age dataset is 1849 years, this is considerably larger than the excess uncertainty for the ¹⁰Be exposure ages (37 years) and suggests additional uncertainty beyond stated analytical uncertainties is contributing towards increased scatter visible in the in situ ¹⁴C dataset.

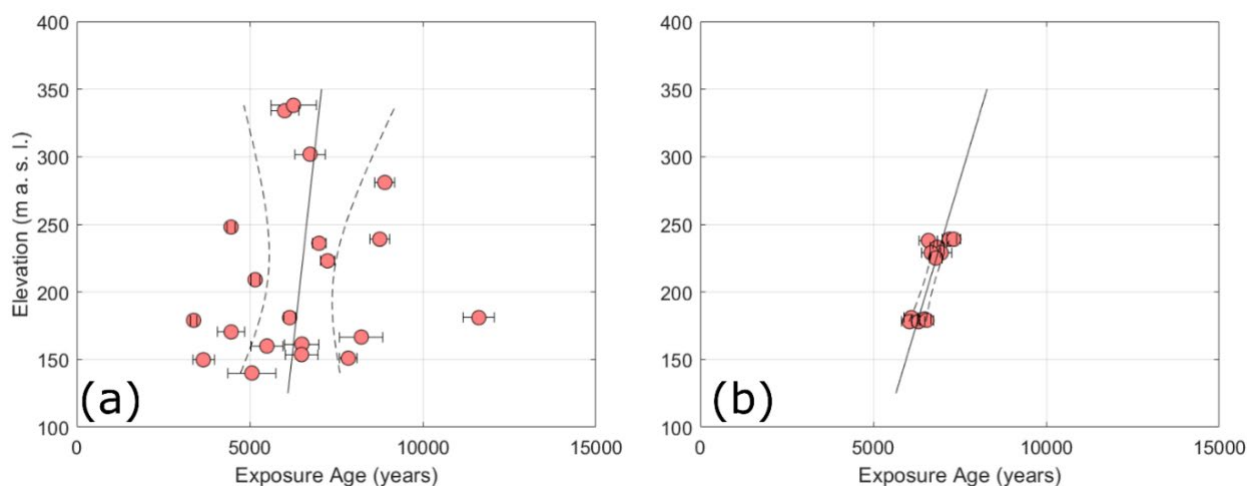


Figure S14: Results of bootstrapped linear regression for Kay Peak/ scoria cone **(a)** in situ ^{14}C dataset ($n=20$) and **(b)** ^{10}Be dataset ($n = 12$). In both panels exposure ages are shown with 1σ internal uncertainties. The solid line in each plot represents the line of best fit determined from linear regression, and the dashed lines represent the 95 % confidence interval. Note ^{10}Be apparent exposure ages strongly suggesting nuclide inheritance (Johnson et al., 2020) were not included in the bootstrapping analysis. Exposure ages presented in both plots have been calculated using the LSDn scaling scheme.

Table S6 Summary statistics of bootstrapping results of in situ ^{14}C derived exposure ages ($n=20$) compared to summary statistics of ^{10}Be exposure ages ($n = 12$) from Kay Peak and scoria cone sites. The purpose of the statistical analysis is to identify unquantified sources of uncertainty. ^{10}Be inheritance is a known contributor to scatter in ^{10}Be measurements so any samples strongly suspected of contributing scatter to the ^{10}Be dataset due to inheritance have been removed.

Reported Metric	^{14}C Kay Peak & scoria cone	^{10}Be Kay Peak & scoria cone
Std Dev. Residuals (yrs)	1957	225
Av. analytical error 1σ (yrs)	641	222
Av. external error 1σ (yrs)	834	453
Error in excess of analytical uncertainty (yrs)	1849	37

4.1.1 A statistical comparison of in situ ^{14}C and ^{10}Be datasets at scoria cone and Kay Peak

The statistical analysis (Table S6) indicates almost all scatter in the distribution of ^{10}Be exposure ages which are of Holocene age and not removed as outliers from scoria cone and Kay Peak sites, can be accounted for by the reported analytical uncertainty in ^{10}Be AMS measurements. This finding is consistent with improvements in AMS precision and reproducibility reported from CRONUS-A and CRONUS-N intercomparison materials (Corbett et al., 2022; Jull et al., 2015). However, uncertainty in excess of measurement uncertainty of the in situ ^{14}C exposure ages (1849 years), exceeds the average in situ ^{14}C measurement uncertainty (641 years) reported for Kay Peak and scoria cone elevation-age datasets (Fig. S14).

Exposure ages for both in situ ^{14}C and ^{10}Be used in our bootstrapping comparison are from the same sample sites: Kay Peak and scoria cone. Very few are however paired ^{14}C - ^{10}Be measurements from the same sample ($n = 3$). Differences in geological scatter of individual samples from both datasets could explain some of the mismatch in excess scatter determined for in situ ^{14}C and ^{10}Be exposure ages. The inclusion of ^{10}Be exposure ages from Kay Peak that pre-date the Holocene would increase scatter in the ^{10}Be profile but represent a recognised

source of ^{10}Be scatter from inheritance. ^{10}Be outliers are generally easier to identify and filter because inheritance can quite obviously increase the apparent exposure age relative to the main population. Scatter observed from the in situ ^{14}C ages is however large relative to the total amount of inheritance or post-depositional disturbance typically detected in an in situ ^{14}C measurement due to the short-half-life mitigating for inheritance over multiple glaciations. The removal of ^{10}Be outliers with inheritance decreases the elevation range of samples used for the ^{10}Be dataset (180–240 m a. s. l.) relative to the in situ ^{14}C dataset (150–350 m a. s. l.). This results in two clustered ^{10}Be age populations from scoria cone, making the ^{10}Be dataset essentially a two-point data fit, resulting in a small 95 % confidence interval. Nevertheless, the difference of ~ 1800 years of excess scatter beyond analytical uncertainty for the in situ ^{14}C exposure age dataset relative to ^{10}Be exposure age dataset is still significant.

To summarise, the in situ ^{14}C and ^{10}Be chronologies are broadly similar with respect to the timing of deglaciation, implying they are equally accurate. There is, however, a significant amount of scatter in the distribution of in situ ^{14}C exposure ages that cannot be accounted for by the nominal 6 % 1σ internal measurement uncertainty for in situ ^{14}C adopted in many studies (Balco et al., 2019; Nichols et al., 2019). In contrast, uncertainty in ^{10}Be analytical measurements can account for the scatter observed in the distribution of Holocene ^{10}Be ages at the site. The two possibilities are 1) unquantified geological scatter is disproportionately impacting in situ ^{14}C exposure ages in the scoria cone and Kay Peak datasets and 2) in situ ^{14}C measurement uncertainty is not fully accounting for uncertainties incorporated during sample preparation.

Supplement S4: Assessment of Mt Murphy quartz separates impact on in situ ^{14}C reproducibility

Mineral elemental impurities which are not fully homogenised within a sample can lead to differences in measured nuclide concentrations, impacting reproducibility (Corbett et al., 2022). In situ ^{14}C production in silicates (such as quartz, typically sampled for ^{10}Be , ^{26}Al and ^{14}C measurements) at SLHL is dominated by oxygen spallation accounting for > 90 % at SLHL, but also occurs from spallation of Si, Mg, Al and Na (Koester and Lifton, 2023). Modelled in situ ^{14}C spallogenic production rates for Mg-rich silicates such as olivine, are 7–10 % lower than pure quartz, while Al-rich minerals such as K and Ca feldspars have production rates 12–13 % below quartz. Modelled in situ ^{14}C production rates for Fe bearing minerals such as fayalite (Fe_2SiO_4) are as much as 41 % lower than pure quartz (Koester and Lifton, 2023). Trace elements or minerals within the quartz mineral separate can therefore cause differences in the in situ ^{14}C production rate, impacting reproducibility. We therefore conduct a preliminary examination to determine if trace elemental impurities of Al, Fe, Mg, Ca, Na, Ti, and K measured in Mt Murphy samples following quartz purification (Table S7) impact the spallogenic in situ ^{14}C production rate and partly account for in situ ^{14}C repeat analyses which do not reproduce within 6 % 1σ (or 2σ) uncertainties.

Table S7: Concentration data measured by ICP-OES of major elemental impurities (displayed as weight %) following quartz purification of samples measured for in situ ^{14}C ($n = 9$). The total sum weight % of elements is displayed, and percentage of each sample which is pure quartz (far right column). This differs from the (Corbett et al., 2022) study which reported elemental analysis results following the majority of Be extraction steps including column chemistry but is appropriate for investigating in situ ^{14}C reproducibility because situ ^{14}C analyses are made directly on in situ ^{14}C gas extracted from the quartz mineral separate.

Sample ID	Al wt %	Fe wt %	Mg wt %	Ca wt %	Na wt %	Ti wt %	K wt %	Total wt %	SiO ₂ wt %
NOT-104	0.0052	0.0006	0.0001	0.0004	0.0003	0.0023	0.0009	0.0098	99.9902
NOT-107	0.0043	0.0005	0.0001	0.0006	0.0006	0.0016	0.0007	0.0084	99.9916
NOT-103	0.0079	0.0006	0.0001	0.0006	0.0002	0.0018	0.0001	0.0113	99.9887
TUR-123	0.0089	0.0001	0.0001	0.0008	0.0004	0.0015	0.0000	0.0118	99.9882
TUR-117	0.0026	0.0001	0.0000	0.0007	0.0009	0.0012	0.0008	0.0063	99.9937
TUR-132	0.0017	0.0014	0.0000	0.0012	0.0003	0.0019	0.0000	0.0065	99.9935
CIN-102	0.0147	0.0056	0.0016	0.0020	0.0009	0.0033	0.0063	0.0344	99.9656
CIN-108	0.0031	0.0003	0.0001	0.0007	0.0003	0.0017	0.0001	0.0063	99.9937
CIN-112	0.0035	0.0003	0.0002	0.0008	0.0006	0.0016	0.0004	0.0074	99.9926

Trace element concentrations in Mt Murphy quartz mineral separates were obtained by Inductively Coupled Plasma Optical Emission Spectrometer (ICP-OES) following quartz purification at Imperial College London. We calculated the equivalent weight % of the oxides Al_2O_3 , Fe_2O_3 , MgO , CaO , Na_2O , TiO_2 , and K_2O in Mt Murphy samples from the ICP-OES elemental concentration data. We used the MATLAB code of Koester and Lifton (2023) to calculate compositionally dependent, site-specific production rates (at $\text{g}^{-1} \text{yr}^{-1}$) for each Mt Murphy sample measured for in situ ^{14}C (Table S7). Our analysis shows that 1) the elemental abundance of the target element impurities in the Mt Murphy mineral separates is extremely low for all samples, i.e., the quartz purity of Mt Murphy samples is high ($> 99.9\%$) (Table S7) and 2) trace elemental impurities that persisted in mineral separates following quartz purification do not significantly impact modelled in situ ^{14}C spallogenic production rates.

Table S8: Comparison of modelled in situ ^{14}C compositionally dependent, site-specific production rates (P_{CD}) for Mt Murphy quartz mineral separates. The in situ ^{14}C production rate calculated with the elemental impurities measured in the quartz minerals by ICP-OES (Table S8) is contrasted to the in situ ^{14}C production rate for the same samples assuming they are compositionally 100 % SiO_2 . Modelled in situ ^{14}C production rates calculated using the LSDn scaling scheme of (Lifton et al., 2014) and code of Koester and Lifton (2023).

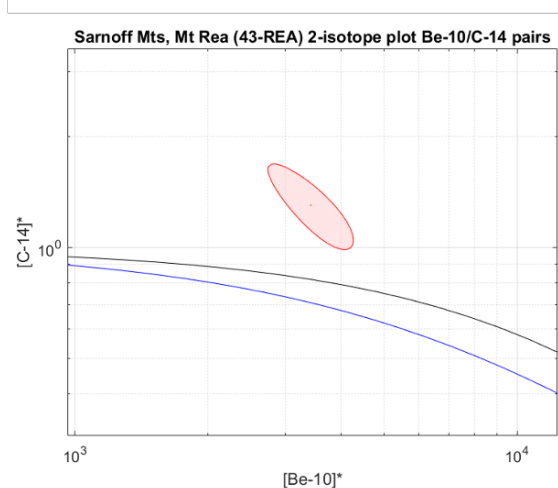
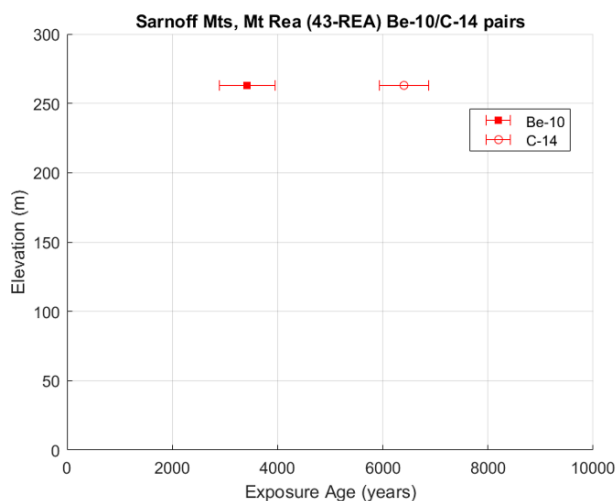
Sample Name	$^{14}\text{C} - ^{10}\text{Be}$	^{14}C Rep. (2σ)	Latitude (DD)	Longitude (DD)	Elevation (m a. s. l.)	^{14}C PCD Diff. (%)
NOT-104	discordant	-	-75.38863	-111.11753	893	100.003
NOT-107	discordant	-	-75.38818	-111.09055	885	100.003
NOT-103	discordant	-	-75.39144	-111.13985	852	100.003
TUR-123	discordant	-	-75.37061	-111.29230	639	100.003
TUR-117	discordant	No	-75.38110	-111.30660	451	100.002
TUR-132	concordant	Yes	-75.38303	-111.30911	446	100.003
CIN-102	concordant	-	-75.21943	-111.02316	239	100.014
CIN-108	concordant	Yes	-75.21652	-111.01973	181	100.002
CIN-112	discordant	No	-75.21628	-111.01796	179	100.002

The maximum difference in the in situ ^{14}C production rate calculated assuming pure SiO_2 and the elemental composition of Mt Murphy samples measured by ICP-OES (Table S8) is 0.014% for sample CIN-102 (this sample also contains the highest total % weight elemental impurities at 0.03 % or 300 ppm). For all other samples the difference in modelled production rates is $< 0.001\%$ (Table S8). Marginal differences in modelled in situ ^{14}C production rates of 0.002–0.014 % therefore do not account for in situ ^{14}C concentrations of Mt Murphy replicate measurements, which are not reproducible using 6 % 1σ uncertainties. This preliminary analysis is limited by the small number of replicate samples ($n = 4$). In addition, only production pathways by in situ ^{14}C by spallation are modelled, while muogenic in situ ^{14}C production at SLHL constitutes ~20% of total production. Nevertheless, our analysis indicates very low elemental impurities detected in Mt Murphy mineral separates results in extremely small changes to the in situ ^{14}C production rate and so does not account for observed scatter of up to 100 % between replicate in situ ^{14}C concentrations from the Mt Murphy dataset. Our evaluation of Mt Murphy samples therefore finds no significant link between low abundances of elemental impurities in quartz mineral separates and in situ ^{14}C reproducibility. Nevertheless, a more in-depth study similar to Corbett et al., (2022) which assessed impact of quartz impurity in CRONUS-N on ^{10}Be reproducibility would help improve quantification of in situ ^{14}C reproducibility. We would, however, suggest a different intercomparison material, e.g., CRONUS-R which is a low-level sample (Fülöp et al., 2019) as being appropriate for this purpose.

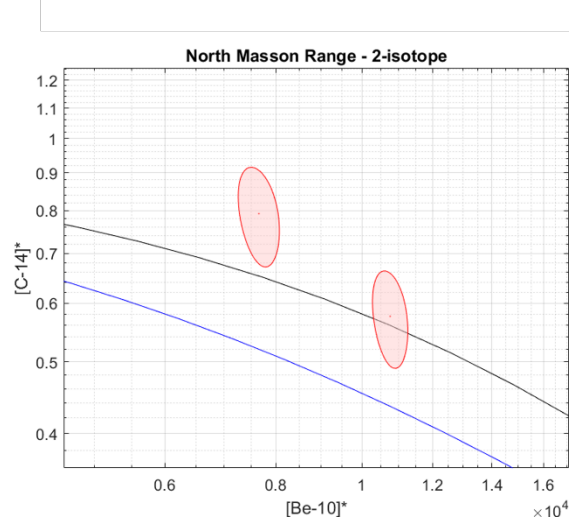
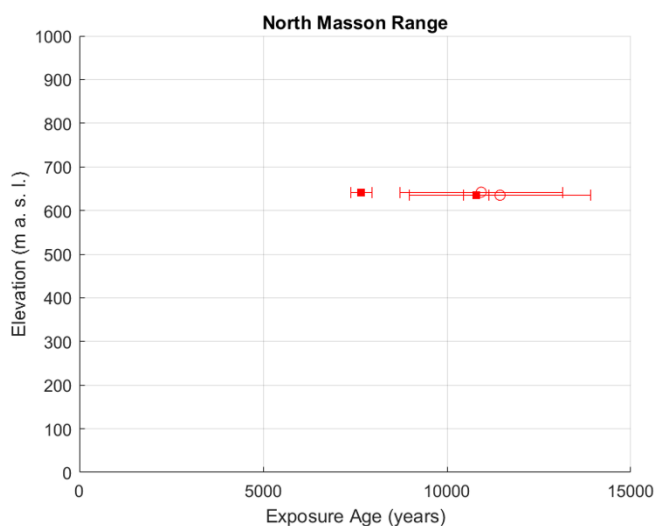
Supplement S5: Holocene filter age vs elevation plots and paired nuclide diagrams.

This supplement contains exposure age vs elevation plots (1σ uncertainties) and paired nuclide diagrams (68% error ellipses) displaying all sites where paired in situ ^{14}C - ^{10}Be exposure ages were extracted from ICE-D [last accessed - 29.03.24] using the Holocene search filter (see main text, Section 3.1). Sites are numbered according to their unique site ID in ICE-D and correspond to numbering in Figure 1, and Table 4 in the main paper. Mt Murphy age vs elevation plots and paired nuclide diagrams (sites 2, 7 and 8) are in the main paper (Fig. 3, Fig. 4).

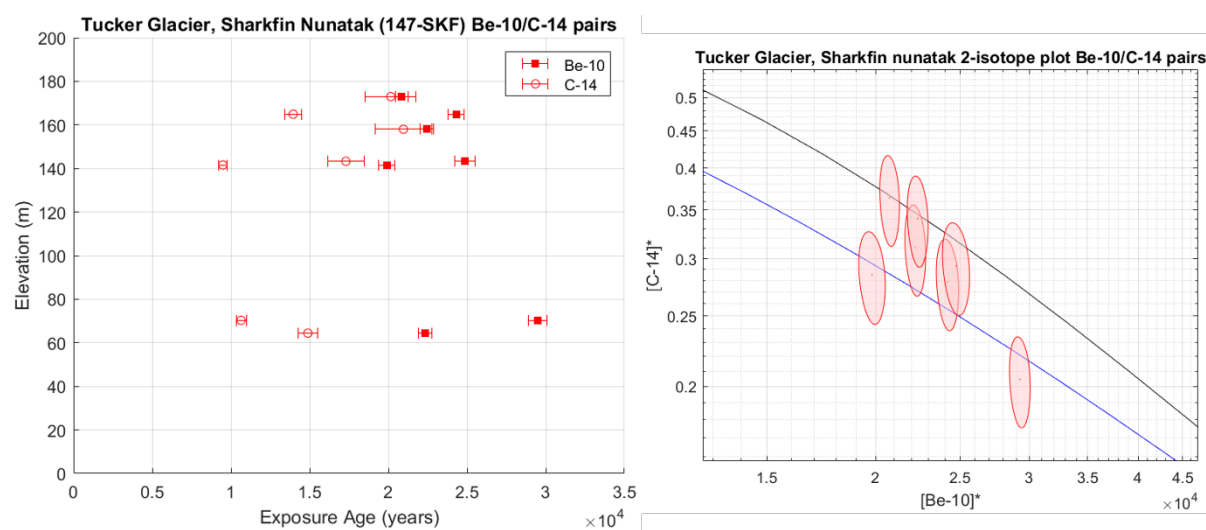
Site 1: Mt Rea, Sarnoff Mts. (Ross Sea) - Type 3



Site 3: North Masson Range, Framnes Mts (East Antarctica) - Type 3 (1)

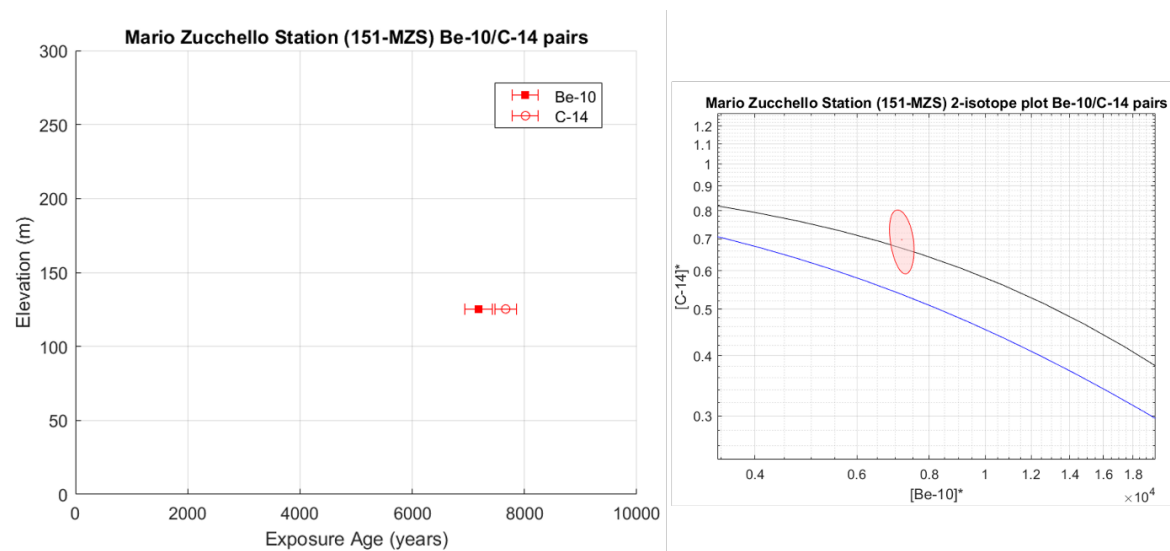


Site 4: Sharkfin nunatak, Tucker Glacier (Ross Sea) - Type 1 (2)

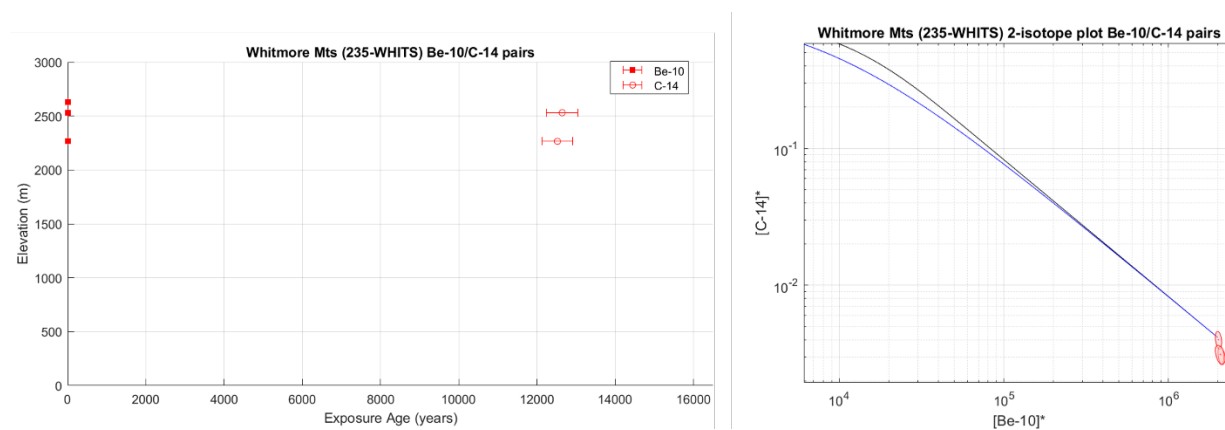


435

Site 5: Mario Zucchelli Station, Terra Nova Bay (Ross Sea) – Type 1

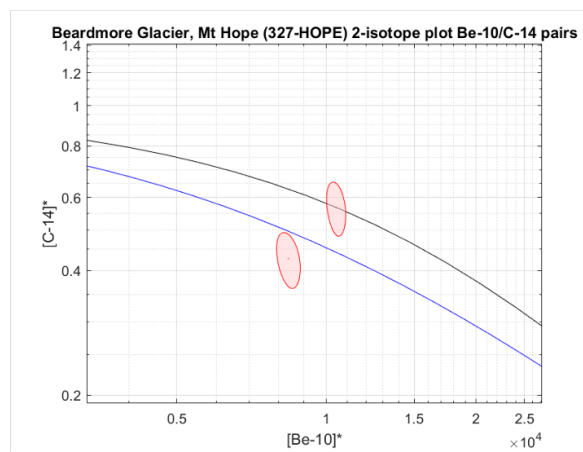
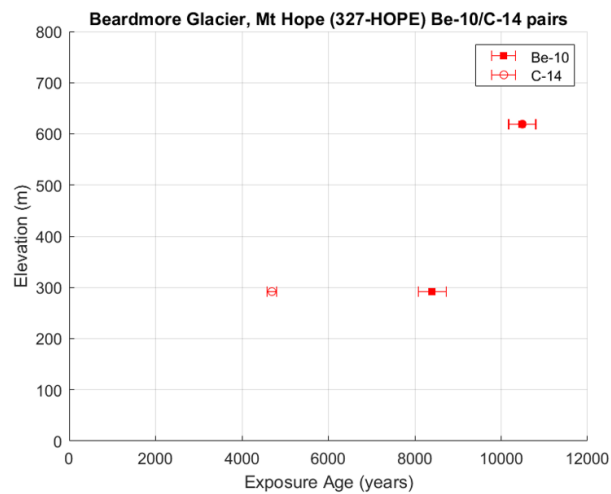


Site 6: Mt Whitmore, Whitmore Mts. (Ross Sea) – Type N/A

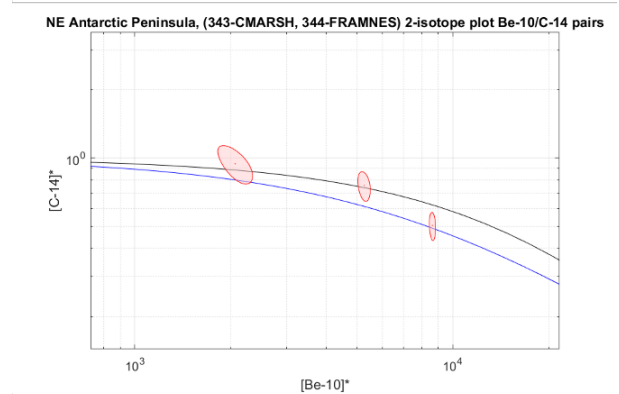
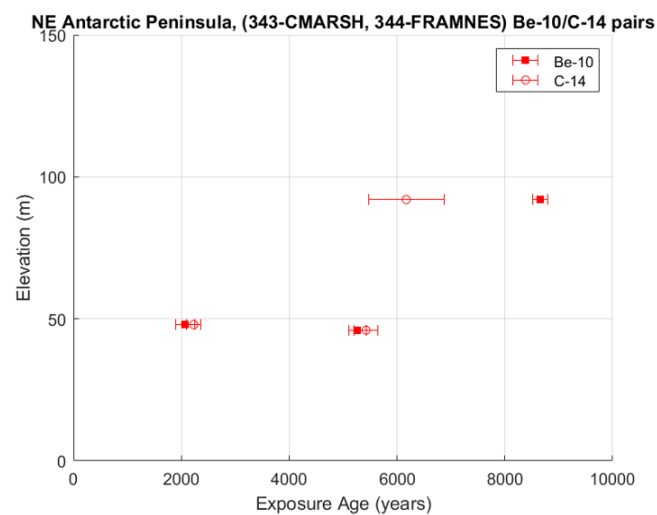


440

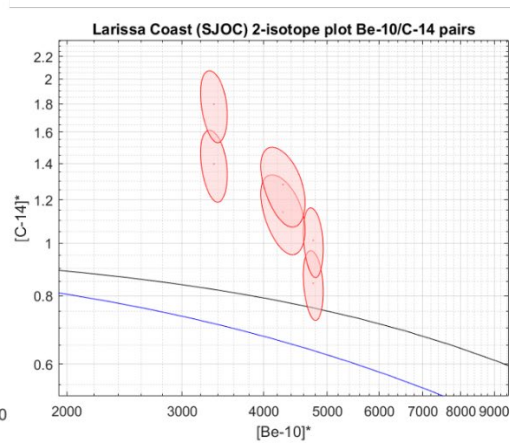
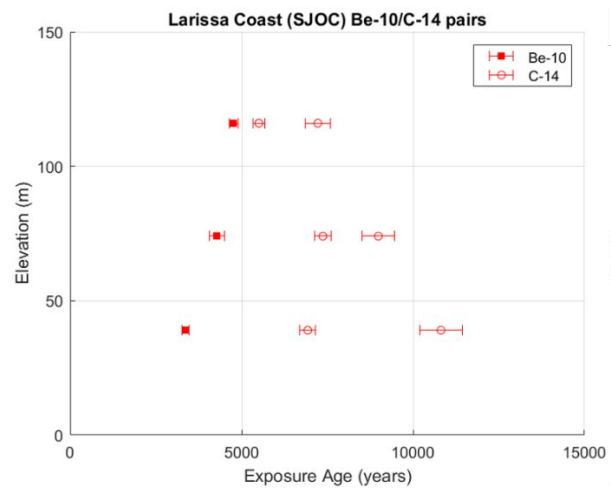
Site 9: Mt Hope, Beardmore Glacier (Ross Sea) – Type 1 2



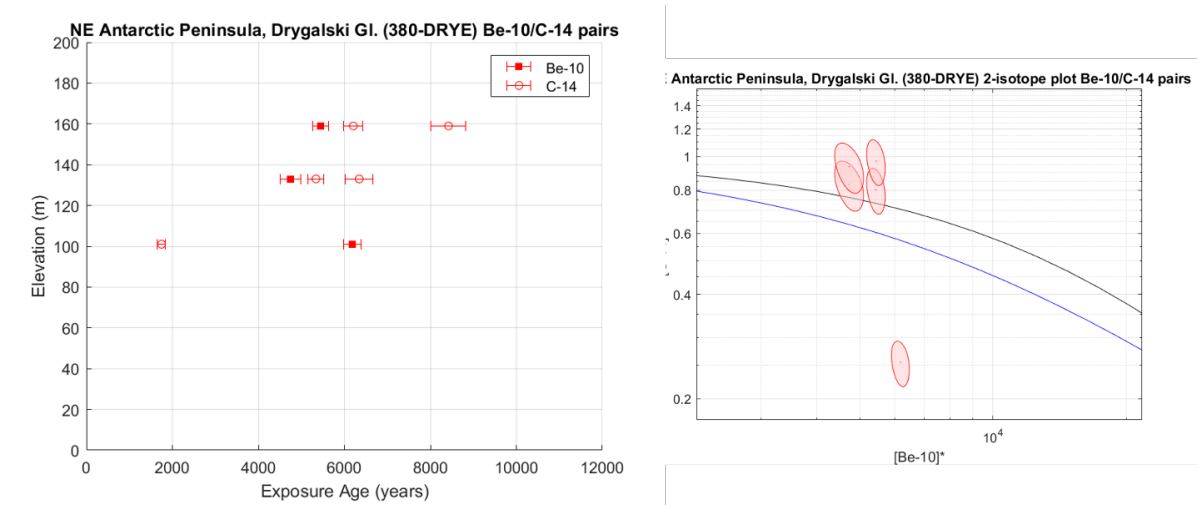
445 Site 10 and Site 11: Cape Marsh and Cape Framnes (Antarctic Peninsula) – Type 1 (2)



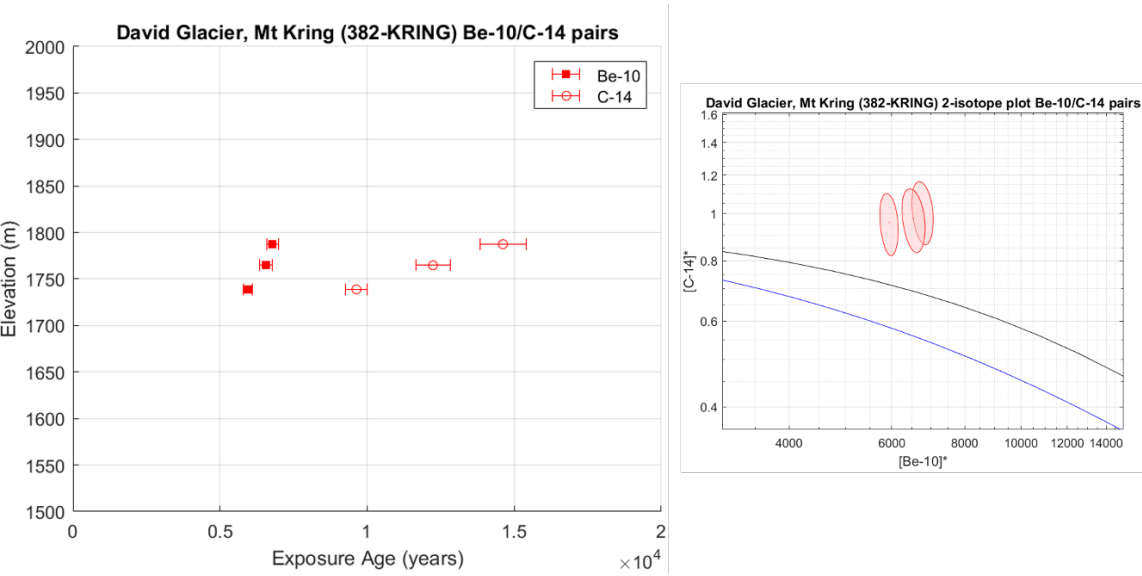
Site 12: Site C, Sjogren-Boydell Fjord (Antarctic Peninsula) – Type 3



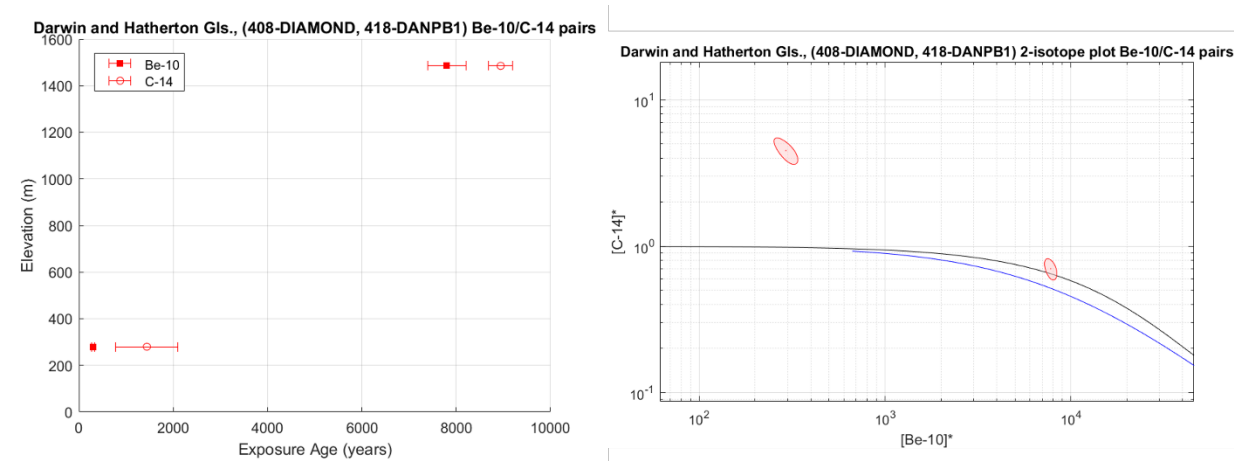
Site 13: Site E, Drygalski Glacier (Antarctic Peninsula) – Type 1 2 3



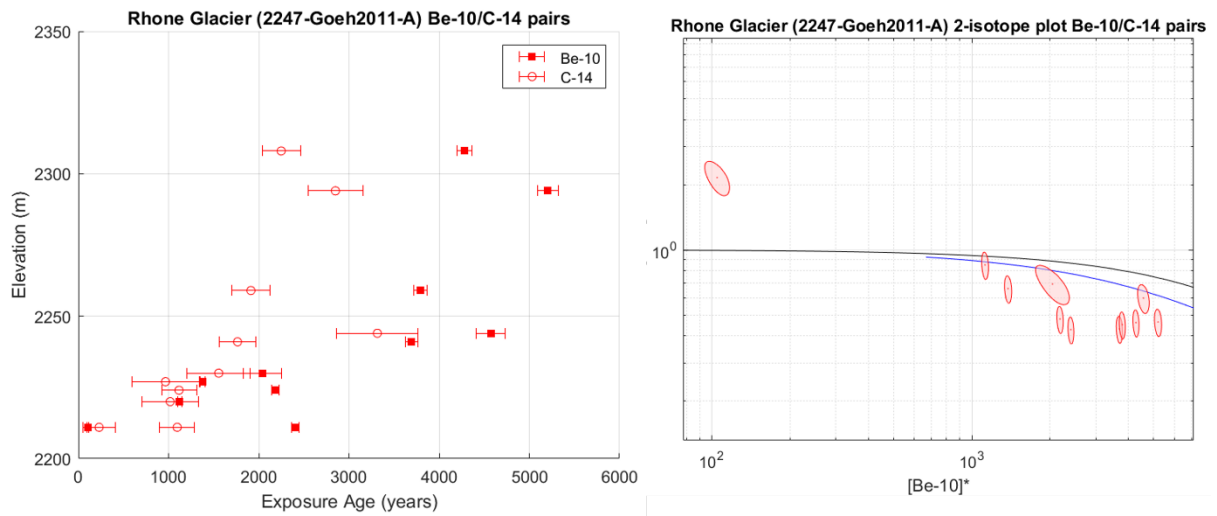
Site 14: Mt Kring, David Glacier (Ross Sea) – Type 3



Site 15 and Site 16: Diamond Hill and Danum Plat., Darwin and Hath. Gl. (Ross Sea) - Type 1, 3

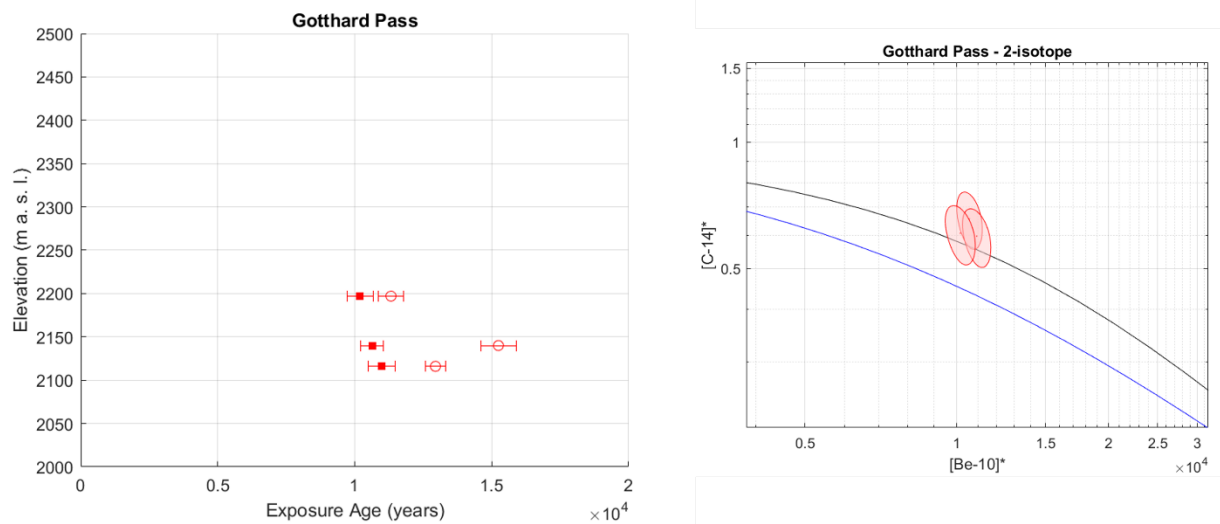


Site 17: Rhone Glacier, Switzerland (Europe) – Type 2

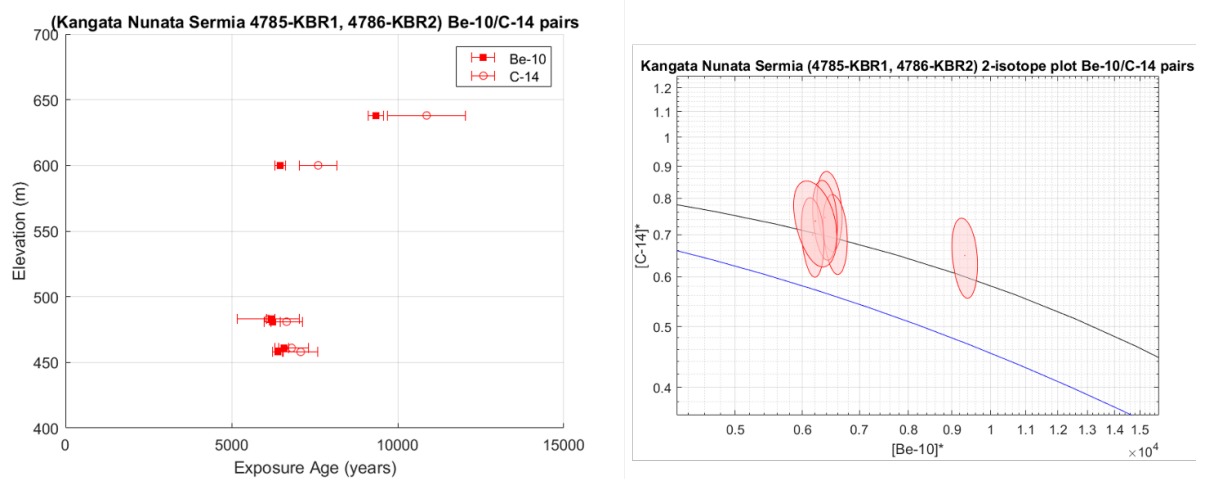


460

Site 18: Gotthard Pass, Switzerland (Europe) – Type 1

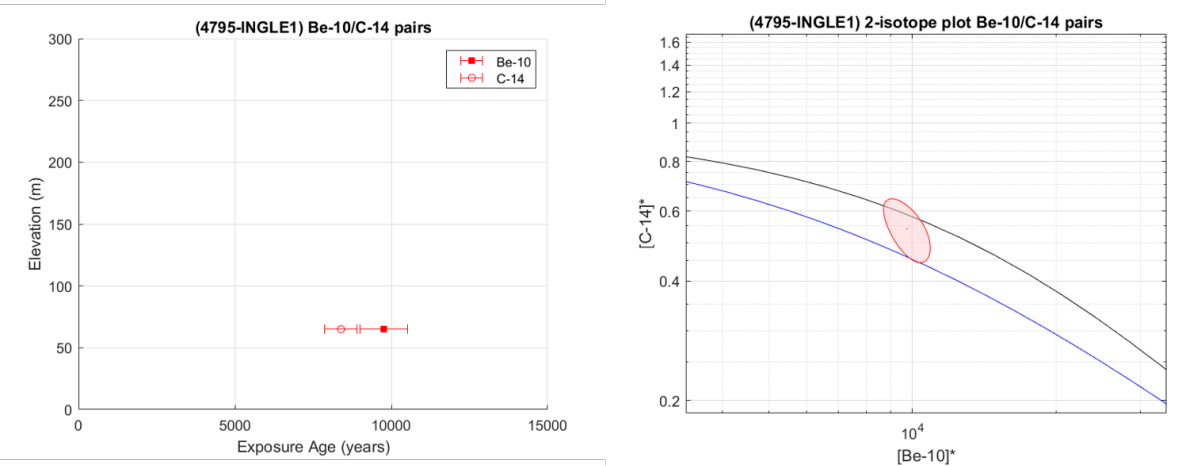


Site 19 and Site 20: Kangata Nunata Sermia, Greenland – Type 1

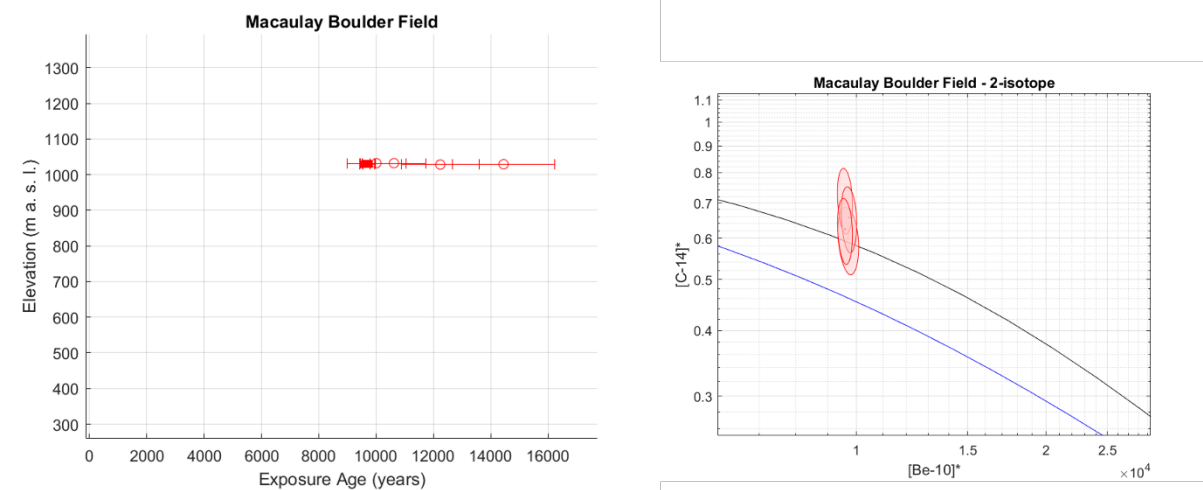


465

Site 21: Outboard of present margin, Inglefield Land (Greenland) – Type 1

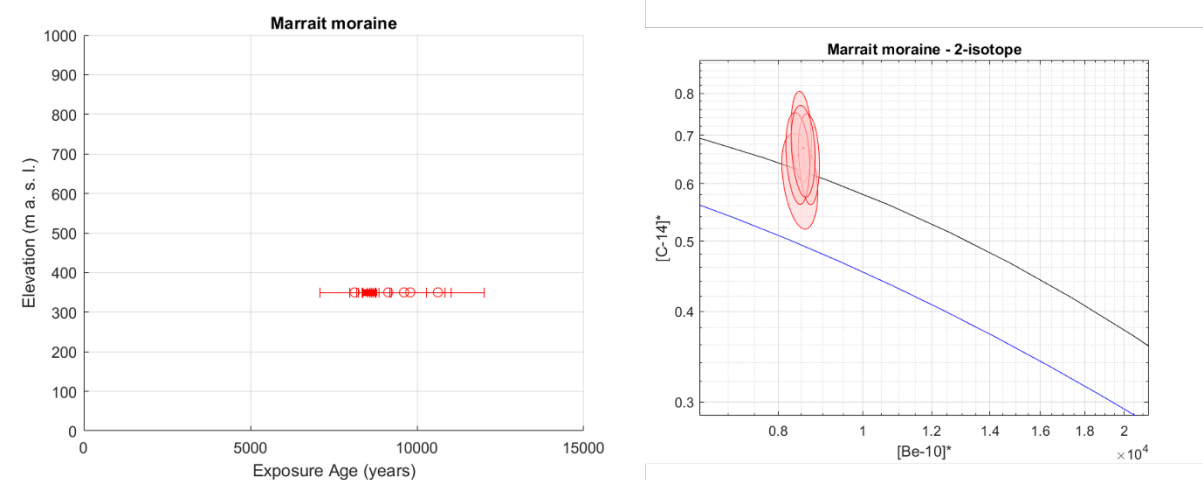


Site 22: Macaulay Boulder Field, Southern Alps (New Zealand) – Type 1

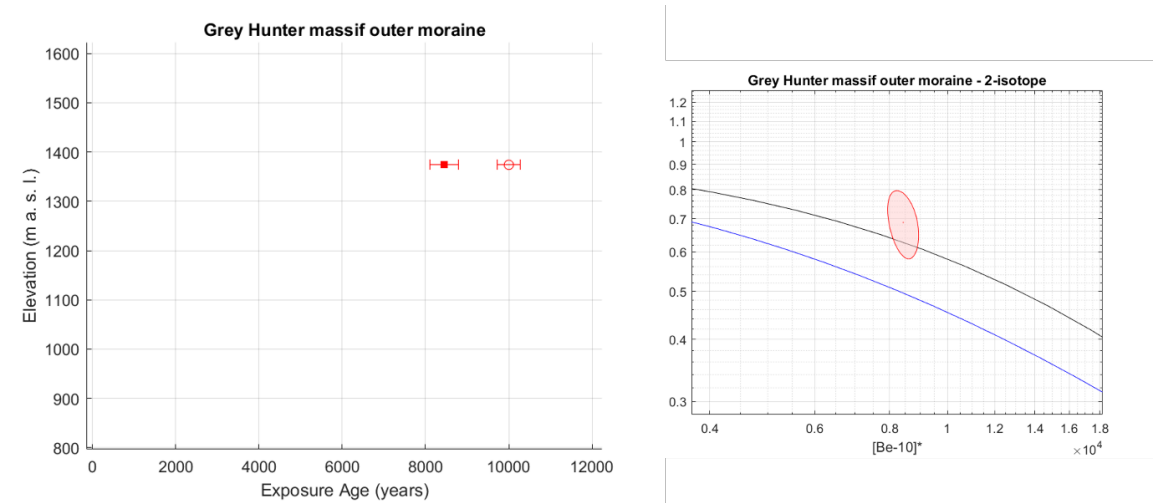


470

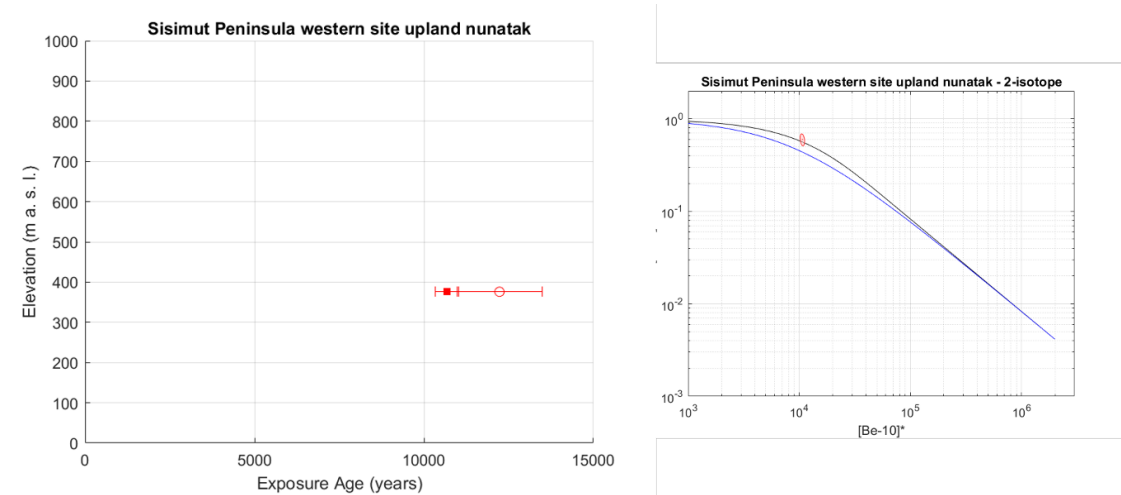
Site 23: Marrait Moraine, Jakobshavn Isfjord (Greenland) – Type 1



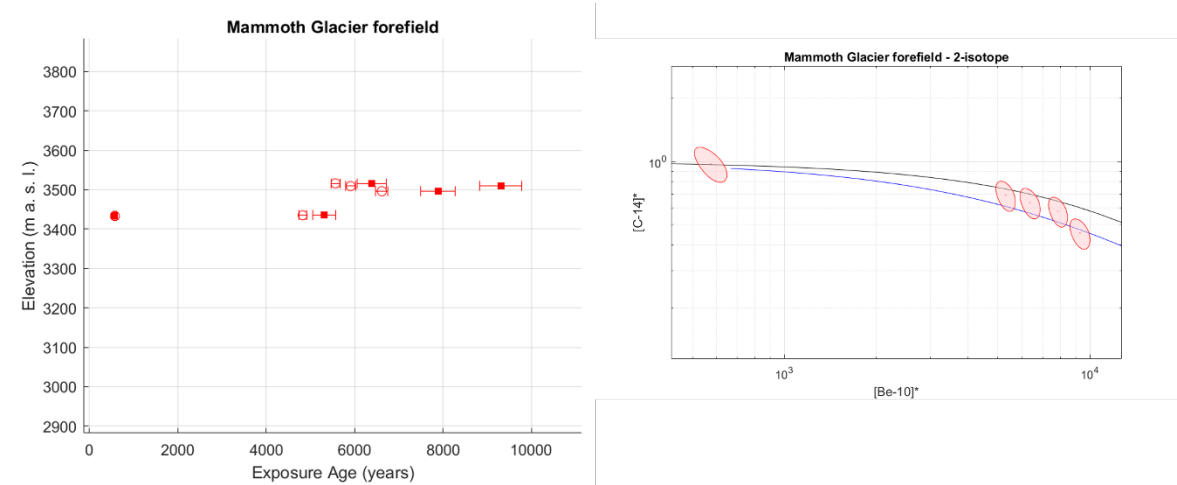
Site 24: Grey Hunter Massif, MacArthur Mts. (Yukon) – Type 1



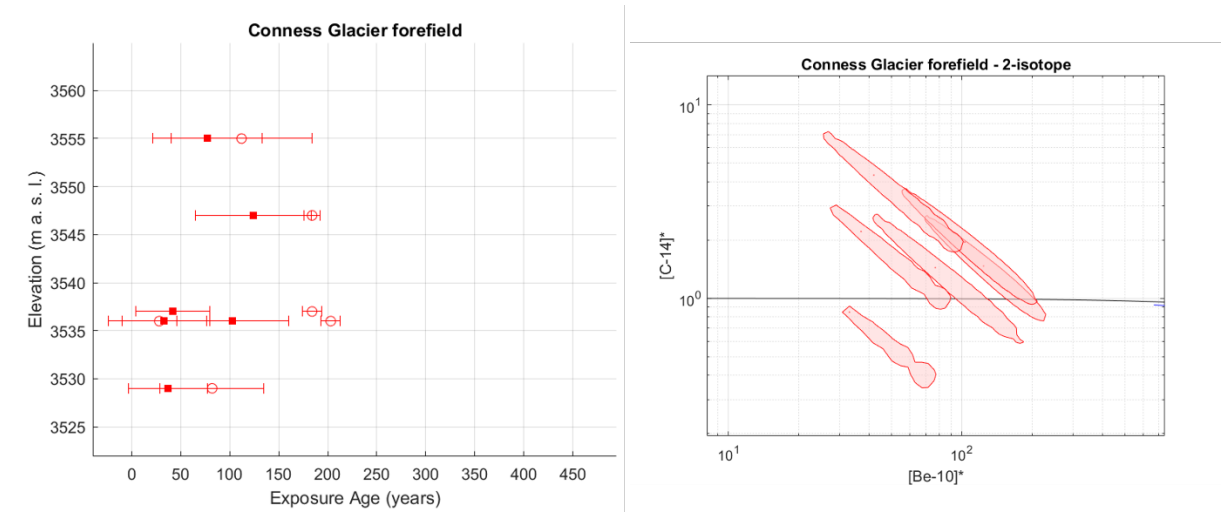
Site 25: Western upland nunatak, Sisimiut Peninsula (Greenland) – Type 1



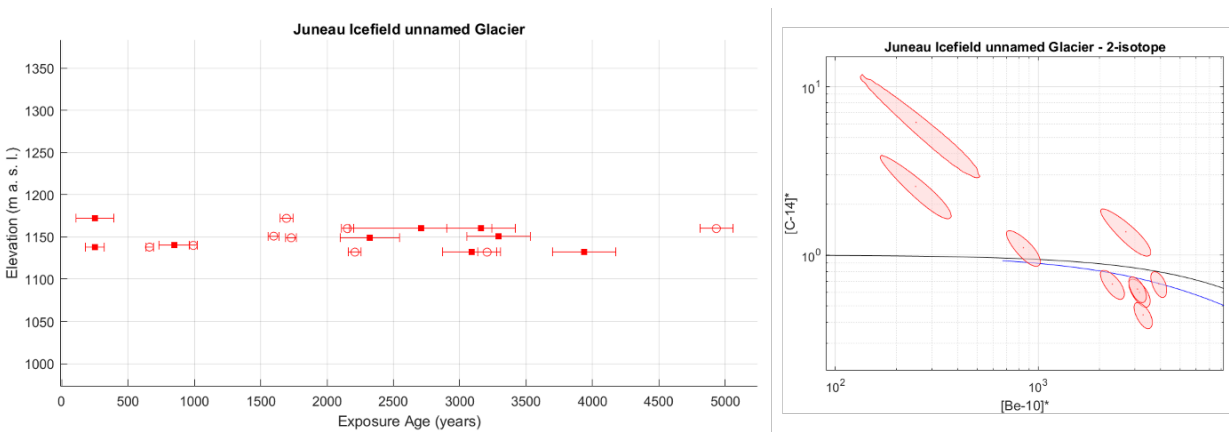
Site 26: Mammoth Glacier forefield, Wind River Range (Wyoming) – Type 1



485 **Site 27: Conness Glacier forefield, Sierra Nevada (California) – Type 1 2 3 (elongate)**



Site 28: Unnamed Glacier, Juneau Ice Field (Alaska) – Type 1 2 3



490

495

500

References – supplementary materials

- Adams, J. R., Johnson, J. S., Roberts, S. J., Mason, P. J., Nichols, K. A., Venturelli, R. A., Wilcken, K., Balco, G., Goehring, B., Hall, B., Woodward, J., and Rood, D. H.: New ^{10}Be exposure ages improve Holocene ice sheet thinning history near the grounding line of Pope Glacier, Antarctica, *The Cryosphere*, 16, 4887–4905, <https://doi.org/10.5194/tc-16-4887-2022>, 2022.
- Balco, G.: Production rate calculations for cosmic-ray-muon-produced ^{10}Be and ^{26}Al benchmarked against geological calibration data, *Quaternary Geochronology*, 39, 150–173, <https://doi.org/10.1016/j.quageo.2017.02.001>, 2017.
- Balco, G. and Schaefer, J. M.: Exposure-age record of Holocene ice sheet and ice shelf change in the northeast Antarctic Peninsula, *Quaternary Science Reviews*, 59, 101–111, <https://doi.org/10.1016/j.quascirev.2012.10.022>, 2013.
- Balco, G., Todd, C., Goehring, B. M., Moening-swanson, I., and Nichols, K.: Glacial geology and cosmogenic-nuclide exposure ages from the Tucker Glacier - Whitehall Glacier confluence, Northern Victoria Land, Antarctica, *American Journal of Science*, 319, 255–286, <https://doi.org/10.2475/04.2019.01>, 2019.
- Balco, G., Brown, N., Nichols, K., Venturelli, R. A., Adams, J., Braddock, S., Campbell, S., Goehring, B., Johnson, J. S., Rood, D. H., Wilcken, K., Hall, B., and Woodward, J.: Reversible ice sheet thinning in the Amundsen Sea Embayment during the Late Holocene, *The Cryosphere*, 17, 1787–1801, 2023.
- Bevington, P. and Robinson, D.: Data reduction and error analysis for the physical sciences, edited by: Bruflodt, D. and Cotkin, Spencer. J., McGraw Hill, New York, 1–313 pp., 1993.
- Burton-Johnson, A., Black, M., Fretwell, P. T., and Kaluza-Gilbert, J.: An automated methodology for differentiating rock from snow, clouds and sea in Antarctica from Landsat 8 imagery: a new rock outcrop map and area estimation for the entire Antarctic continent, *The Cryosphere*, 10, 1665–1677, <https://doi.org/10.5194/tc-10-1665-2016>, 2016.
- Corbett, L. B., Bierman, P. R., Brown, T. A., Caffee, M. W., Fink, D., Freeman, S. P. H. T., Hidy, A. J., Rood, D. H., Wilcken, K. M., and Woodruff, T. E.: Clean quartz matters for cosmogenic nuclide analyses: An exploration of the importance of sample purity using the CRONUS-N reference material, *Quaternary Geochronology*, 73, 101403, <https://doi.org/10.1016/j.quageo.2022.101403>, 2022.
- Dunai, T. J.: Cosmogenic nuclides: Principles, concepts and applications in the earth surface sciences, 1–187 pp., <https://doi.org/10.1017/CBO9780511804519>, 2010.
- Fülöp, R.-H., Fink, D., Yang, B., Codilean, A. T., Smith, A., Wacker, L., Levchenko, V., and Dunai, T. J.: The ANSTO – University of Wollongong in-situ ^{14}C extraction laboratory, *Nuclear Instruments and Methods in Physics Research Section B: Beam Interactions with Materials and Atoms*, 438, 207–213, <https://doi.org/10.1016/j.nimb.2018.04.018>, 2019.
- Goehring, B. M., Schaefer, J. M., Schluechter, C., Lifton, N. A., Finkel, R. C., Jull, A. J. T., Akçar, N., and Alley, R. B.: The Rhone Glacier was smaller than today for most of the Holocene, *Geology*, 39, 679–682, <https://doi.org/10.1130/G32145.1>, 2011.
- Goehring, B. M., Balco, G., Todd, C., Moening-Swanson, I., and Nichols, K.: Late-glacial grounding line retreat in the northern Ross Sea, Antarctica, *Geology*, 47, 291–294, <https://doi.org/10.1130/G45413.1>, 2019.
- Heisinger, B., Lal, D., Jull, A. J. T., Kubik, P., Ivy-Ochs, S., Knie, K., and Nolte, E.: Production of selected cosmogenic radionuclides by muons: 2. Capture of negative muons, *Earth and Planetary Science Letters*, 200, 357–369, [https://doi.org/10.1016/S0012-821X\(02\)00641-6](https://doi.org/10.1016/S0012-821X(02)00641-6), 2002.
- Jeong, A., Il, J., Bae, Y., Balco, G., Yoo, K., Il, H., Domack, E., Hee, H., and Yong, B.: Late Quaternary deglacial history across the Larsen B embayment, Antarctica, *Quaternary Science Reviews*, 189, 134–148, <https://doi.org/10.1016/j.quascirev.2018.04.011>, 2018.

- 545 Johnson, J. S., Roberts, S. J., Rood, D. H., Pollard, D., Schaefer, J. M., Whitehouse, P. L., Ireland, L. C., Lamp, J. L., Goehring, B. M., Rand, C., and Smith, J. A.: Deglaciation of Pope Glacier implies widespread early Holocene ice sheet thinning in the Amundsen Sea sector of Antarctica, *Earth and Planetary Science Letters*, 548, 116–501, <https://doi.org/10.1016/j.epsl.2020.116501>, 2020.
- 550 Jull, A. J. T., Scott, E. M., and Bierman, P.: The CRONUS-Earth inter-comparison for cosmogenic isotope analysis, *Quaternary Geochronology*, 26, 3–10, <https://doi.org/10.1016/j.quageo.2013.09.003>, 2015.
- Koester, A. J. and Lifton, N. A.: Technical note: A software framework for calculating compositionally dependent in situ ^{14}C production rates, *Geochronology*, 5, 21–33, <https://doi.org/10.5194/gchron-5-21-2023>, 2023.
- 555 Lamp, J. L., Young, N. E., Koffman, T., Schimmelpfennig, I., Tuna, T., Bard, E., and Schaefer, J. M.: Update on the cosmogenic in situ ^{14}C laboratory at the Lamont-Doherty Earth Observatory, *Nuclear Instruments and Methods in Physics Research, Section B: Beam Interactions with Materials and Atoms*, 456, 157–162, <https://doi.org/10.1016/j.nimb.2019.05.064>, 2019.
- 560 Lifton, N., Sato, T., and Dunai, T. J.: Scaling in situ cosmogenic nuclide production rates using analytical approximations to atmospheric cosmic-ray fluxes, *Earth and Planetary Science Letters*, 386, 149–160, <https://doi.org/10.1016/j.epsl.2013.10.052>, 2014.
- Milillo, P., Rignot, E., Rizzoli, P., Scheuchl, B., Mouginot, J., Bueso-Bello, J. L., Prats-Iraola, P., and Dini, L.: Rapid glacier retreat rates observed in West Antarctica, *Nature Geoscience*, 15, 48–53, <https://doi.org/10.1038/S41561-021-00877-Z>, 2022.
- 565 Mouginot, J., Scheuchl, B., and Rignot, E.: Mapping of Ice Motion in Antarctica Using Synthetic-Aperture Radar Data, *Remote Sensing*, 4, 2753–2767, <https://doi.org/10.3390/rs4092753>, 2012.
- Mouginot, J., Rignot, E., Scheuchl, B., and Millan, R.: Comprehensive annual ice sheet velocity mapping using Landsat-8, Sentinel-1, and RADARSAT-2 data, *Remote Sensing*, 9, 1–20, <https://doi.org/10.3390/rs9040364>, 2017.
- 570 Nichols, K. A., Goehring, B. M., Balco, G., Johnson, J. S., Hein, A. S., and Todd, C.: New Last Glacial Maximum ice thickness constraints for the Weddell Sea Embayment, Antarctica, *The Cryosphere*, 13, 2935–2951, <https://doi.org/10.5194/tc-13-2935-2019>, 2019.
- Rand, C. and Goehring, B. M.: The distribution and magnitude of subglacial erosion on millennial timescales at Engabreen, Norway, *Annals of Glaciology*, 1–9, 2019.
- 575 Rignot, E., Mouginot, J., and Scheuchl, B.: Antarctic grounding line mapping from differential satellite radar interferometry, *Geophysical Research Letters*, 38, 1–6, <https://doi.org/10.1029/2011GL047109>, 2011a.
- Rignot, E., Mouginot, J., and Scheuchl, B.: Ice flow of the antarctic ice sheet, *Science*, 333, 1427–1430, <https://doi.org/10.1126/science.1208336>, 2011b.
- 580 Simões Pereira, P., van de Flierdt, T., Hemming, S. R., Hammond, S. J., Kuhn, G., Brachfeld, S., Doherty, C., and Hillenbrand, C. D.: Geochemical fingerprints of glacially eroded bedrock from West Antarctica: Detrital thermochronology, radiogenic isotope systematics and trace element geochemistry in Late Holocene glacial-marine sediments, *Earth-Science Reviews*, 182, 204–232, <https://doi.org/10.1016/j.earscirev.2018.04.011>, 2018.
- Young, N. E., Schaefer, J. M., Goehring, B., Lifton, N., Schimmelpfennig, I., and Briner, J. P.: West Greenland and global in situ ^{14}C production-rate calibrations, *Journal of Quaternary Science*, 29, 401–406, <https://doi.org/10.1002/jqs.2717>, 2014.
- 585 Young, N. E., Lesnek, A. J., Cuzzzone, J. K., Briner, J. P., Badgeley, J. A., Balter-Kennedy, A., Graham, B. L., Cluett, A., Lamp, J. L., Schwartz, R., Tuna, T., Bard, E., Caffee, M. W., Zimmerman, S. R. H., and Schaefer, J. M.: In situ cosmogenic ^{10}Be - ^{14}C - ^{26}Al measurements from recently deglaciated bedrock as a new tool to decipher changes in Greenland Ice Sheet size, *Climate of the Past*, 17, 419–450, <https://doi.org/10.5194/cp-17-419-2021>, 2021.

